

# The Rapid Intensification and Eyewall Replacement Cycles of Hurricane Irma (2017)

MICHAEL S. FISCHER, ROBERT F. ROGERS, AND PAUL D. REASOR

*NOAA/Atlantic Oceanographic and Meteorological Laboratory/Hurricane Research Division, Miami, Florida*

(Manuscript received 7 June 2019, in final form 17 December 2019)

## ABSTRACT

The initiation of a rapid intensification (RI) event for a tropical cyclone (TC) at major hurricane intensity is a rare event in the North Atlantic basin. This study examined the environmental and vortex-scale processes related to such an RI event observed in Hurricane Irma (2017) using a combination of flight-level and airborne radar aircraft reconnaissance observations, microwave satellite observations, and model environmental analyses. The onset of RI was linked to an increase in sea surface temperatures and ocean heat content toward levels more commonly associated with North Atlantic RI episodes. Remarkably, Irma's RI event comprised two rapidly evolving eyewall replacement cycle (ERC) episodes that each completed in less than 12 h. The two ERC events displayed different secondary eyewall formation (SEF) mechanisms and vortex evolutions. During the first SEF event, a secondary maximum in ascent and tangential wind was observed at the leading edge of a mesoscale descending inflow jet. During the ensuing ERC event, the primary eyewall weakened and ultimately collapsed, resulting in a brief period of weakening. The second SEF event displayed characteristics consistent with unbalanced boundary layer dynamics. Additionally, it is plausible that both SEF events were affected by the stagnation and axisymmetrization of outward-propagating vortex Rossby waves. During the second ERC event, the TC continued to rapidly intensify, which is a stark contrast to the ERC paradigm described in the literature. The differing ERC evolutions appear linked to the vortex response to changing environmental conditions. The results presented here underscore the utility of frequent aircraft reconnaissance observations for an improved understanding of TC dynamics.

## 1. Introduction

Although the quest for improving tropical cyclone (TC) intensity forecasts has yielded some small, but consistent improvements (DeMaria et al. 2014), TC intensity prediction continues to struggle to accurately predict events of rapid intensification (RI; Gall et al. 2013; Kaplan et al. 2015; Rozoff et al. 2015). Part of this challenge exists because the rate of TC intensification depends on the interaction of processes that occur across a spectrum of spatial and temporal scales, ranging from stochastic, convective-scale processes (e.g., Judt and Chen 2016), to synoptic-scale environmental conditions, which may include external forcing for convection (e.g., Bosart et al. 2000; Kaplan et al. 2015; Fischer et al. 2017). Additionally, despite an improved understanding of the environmental conditions favorable for TC intensification, the environments of RI events have

been shown to be, in large part, statistically similar to TCs that intensify more gradually (Hendricks et al. 2010). As a result, previous work has hypothesized internal dynamics primarily govern whether a given TC will undergo a period of RI, provided a favorable environment exists (Hendricks et al. 2010). The inherent decreased predictability related to such internal processes exacerbates the TC intensity prediction challenge (Judt and Chen 2016).

The intensity of mature TCs is also modulated by internal dynamics via eyewall replacement cycles (ERCs; Willoughby et al. 1982; Black and Willoughby 1992; Sitkowski et al. 2011; Kossin and DeMaria 2016). During a typical ERC, as the outer eyewall develops, the inner eyewall will contract toward the center of the TC, while the storm experiences a period of intensification (Sitkowski et al. 2011). As the outer eyewall intensifies, the inner eyewall begins to decay, resulting in a temporary period of weakening. This period of weakening can occur despite otherwise favorable environmental conditions. Eventually, the outer eyewall intensifies to a

---

*Corresponding author:* Michael S. Fischer, michael.fischer@noaa.gov

point where its tangential wind exceeds that of the inner eyewall, and the TC experiences a period of re-intensification. The end result is a broader TC vortex, which can have important implications on potential TC impacts, such as increasing the area of damaging winds and storm surge (Irish et al. 2008; Lin et al. 2014).

Recent work has allowed for a better understanding of the characteristics of ERC events and, in turn, more accurate TC intensity forecasts. Sitkowski et al. (2011) created a climatology of 24 ERC events in the North Atlantic basin using aircraft reconnaissance observations. Building off this climatology, Kossin and Sitkowski (2012) and Kossin and DeMaria (2016) created statistical TC intensity prediction models containing parameters related to the presence of secondary eyewalls. Kossin and DeMaria (2016) found including such parameters can decrease short-term forecast (i.e., <24 h) errors of operational statistical models by over 50%, with the caveat of a relatively small sample size.

Despite the advances made in understanding and forecasting ERCs, the mechanisms by which a secondary eyewall forms in the first place are less clear, as multiple hypotheses have been put forth. Some of these hypotheses depend on processes internal to the TC. One potential mechanism for secondary eyewall formation (SEF) involves the presence of vortex Rossby waves (VRWs), which propagate along the TC's negative radial vorticity gradient. Montgomery and Kallenbach (1997) linked the outward propagation, and eventual axisymmetrization, of spiral rainbands to VRWs. These outward propagating waves converged at a stagnation radius, where they acted to induce a secondary tangential wind maximum through wave-mean-flow interactions. Using high-resolution simulations of Hurricanes Katrina (2005) and Rita (2005), Abarca and Corbosiero (2011) analyzed convective evolutions consistent with VRW activity, with SEF occurring near the hypothesized VRW stagnation radius. Alternatively, Judt and Chen (2010) assessed a separate simulation of Rita and proposed the presence of a moat region prevented the outward propagation of VRWs. Because SEF was still simulated, Judt and Chen (2010) hypothesized VRWs are not a necessary ingredient for SEF. The importance of a TC's radial vorticity profile for SEF was also emphasized by Terwey and Montgomery (2008), who argued SEF occurs via the axisymmetrization and upscale cascade of vorticity from rainband convection within a region associated with a weak radial gradient of vorticity, referred to as a "beta skirt." Previous observational studies have also noted the presence of a beta skirt prior to SEF (e.g., Dougherty et al. 2018).

Other possible pathways to SEF involve negatively buoyant downdrafts, largely driven by stratiform

precipitation in the downwind end of spiral rainbands. The evaporational cooling associated with stratiform precipitation can create a lower-tropospheric frontal zone between the eyewall and rainband region (Fang and Zhang 2012; Rozoff et al. 2012). This frontal zone facilitates the development of deep convection, which may axisymmetrize to form a secondary eyewall. Alternatively, the evaporational cooling of hydrometeors precipitating from the anvil exhaust of the primary eyewall have been hypothesized to lead a different type of top-down pathway to SEF (Tyner et al. 2018). Observational analyses of aircraft reconnaissance radar observations conducted by Didlake and Houze (2013b) and Didlake et al. (2018) identified instances of a mesoscale descending inflow jet, which ultimately terminated near the top of the TC boundary layer along the inner edge of a region of stratiform precipitation. Near the location where the descending inflow jet reached the entropy-rich TC boundary layer, a region of convergence and intense updrafts was observed, which preceded a local enhancement of the tangential wind field, a developing local secondary circulation, and SEF (Didlake et al. 2018).

Additional boundary layer processes have been hypothesized to be an integral part of SEF. Multiple studies have advocated for the importance of unbalanced dynamics in the generation of a secondary eyewall (Huang et al. 2012; Abarca and Montgomery 2013; Abarca et al. 2016; Huang et al. 2018). In this view, SEF begins with a broadening of the TC vortex and the associated tangential wind field. Thereafter, boundary layer inflow and convergence increase near the location of SEF, within a region of agradient forcing. As the inflow strengthens, the agradient force induces supergradient flow and ascent out of the boundary layer, within a thermodynamically favorable location for convection. Some debate exists, however, about the role of supergradient flow in SEF. Using three diagnostic boundary layer models, Kepert (2013) argued that a broad expansion of the tangential wind field does not necessarily cause a local frictional updraft. Additionally, Kepert (2013) concludes supergradient flow is a by-product of frictional convergence and is not critical to SEF. Instead, it is hypothesized SEF is the result of a feedback between an Ekman-like boundary layer response to a perturbation in the radial gradient of the gradient wind vorticity. Ascent out of the top of the boundary layer, near the location of the vorticity perturbation is presumed to cause a generation of additional vorticity through which the feedback process manifests. Alternatively, Montgomery et al. (2014a) argued agradient forcing in the boundary layer is an essential part of SEF and described multiple limitations

of the [Kepert \(2013\)](#) study. In particular, [Montgomery et al. \(2014a\)](#) discovered the linearized diagnostic boundary layer model of [Kepert \(2013\)](#) poorly replicated the TC structure of two different full-physics, three-dimensional simulations of SEF. [Kepert and Nolan \(2014\)](#) provided a rebuttal to the concerns raised by [Montgomery et al. \(2014a\)](#), but also emphasized nonlinear boundary layer processes in SEF.

Other studies have attributed SEF to external, environmental forcings. For example, upper-tropospheric troughs have been hypothesized to initiate convection radially outward of the primary eyewall, which may cause SEF ([Molinari and Vollaro 1989, 1990](#); [Nong and Emanuel 2003](#); [Leroux et al. 2013](#); [Dai et al. 2017](#)). Similarly, environmental vertical wind shear has been hypothesized to induce asymmetric rainband activity, which may axisymmetrize, resulting in SEF ([Zhang et al. 2017](#); [Dougherty et al. 2018](#)).

Motivated by the important operational and research challenges RI, ERCs, and SEF pose, this study examines the evolution of an RI event in Hurricane Irma (2017) that features two rapidly evolving ERC events. The environmental, vortex, and convective-scale evolutions related to the RI event are examined using flight-level and tail Doppler aircraft reconnaissance observations, passive microwave satellite data, and model analyses of the environment. Here, we will show that the two ERC events are associated with different vortex evolutions and pathways to SEF, despite occurring within 24 h from another.

## 2. Datasets and methods

This study primarily utilized aircraft reconnaissance observations obtained from four Air Force WC-130 and five NOAA WP-3D (P3) missions into Hurricane Irma between 3 and 6 September 2017 ([Table 1](#)). In addition to the in situ measurements taken by the aircraft, each of the five P3 flights sampled the TC using both the C-band lower-fuselage (LFR) radar and the X-band Tail Doppler radar (TDR) onboard the aircraft. The LFR has the advantage of greater resiliency to attenuation and observations are stored at a greater temporal resolution than observations from the TDR. Alternatively, the dual-Doppler TDR is able to retrieve the three-dimensional kinematic structure of the TC vortex. Before the TDR observations were analyzed, they underwent an automated quality control and dealiasing procedure, which produces errors comparable to manual reprocessing ([Rogers et al. 2012](#)). The three-dimensional wind field was retrieved using a similar variational technique to those described in [Gao et al. \(1999\)](#) and [Reasor et al. \(2009\)](#). For each pass the aircraft made through the

TABLE 1. Details of the Air Force WC-130 and NOAA P3 flights analyzed within this study. The maximum sustained 10-m wind ( $V_{\max}$ ;  $\text{m s}^{-1}$ ) and minimum sea level pressure ( $p$ ; hPa) are taken from the nearest best track entry. NOAA P3 flights are indicated by the boldface text.

Mission ID	Approximate initial fix	Approximate final fix	$V_{\max}$ ( $\text{m s}^{-1}$ )	$p$ (hPa)
<b>20170903H1</b>	2100 UTC 3 Sep	0000 UTC 4 Sep	51.4	959
<b>20170904H1</b>	0900 UTC 4 Sep	1300 UTC 4 Sep	56.6	945
20170904U1	1700 UTC 4 Sep	1900 UTC 4 Sep	59.2	944
<b>20170904H2</b>	2200 UTC 4 Sep	0200 UTC 5 Sep	64.3	943
20170904U2	2300 UTC 4 Sep	0500 UTC 5 Sep	64.3	943
<b>20170905H1</b>	1000 UTC 5 Sep	1300 UTC 5 Sep	77.2	929
20170905U1	1100 UTC 5 Sep	1700 UTC 5 Sep	77.2	929
<b>20170905H2</b>	2200 UTC 5 Sep	0000 UTC 6 Sep	79.7	915
20170905U2	2300 UTC 5 Sep	0500 UTC 6 Sep	79.7	915

center of the storm, the observed wind field is solved onto a Cartesian grid with a horizontal resolution of 2 km and a vertical resolution of 0.5 km. Radar observations are available within a  $\sim 75$ –100-km wide swath, centered along the flight track, with some intermittent gaps due to either a lack of scatterers, quality control, or attenuation. The length of most radial legs flown through the TC were between 150 and 180 km.

Once the three-dimensional winds were obtained, the data were interpolated onto a TC-centered cylindrical grid, with a radial, azimuthal, and vertical grid spacing of 1 km,  $1^\circ$ , and 0.5 km, respectively, for each pass the aircraft made through the TC center. The TC center was identified following a technique similar to [Reasor and Eastin \(2012\)](#). In essence, an iterative process was employed, where the TC center was determined to be the point where the azimuthally averaged tangential wind was maximized within annuli of varying widths, ranging from 3 to 13 km, at a height of 2 km. Thereafter, the mean TC center latitude and longitude obtained from the multiple annuli examined were used to determine the “new” TC center.

## 3. Synoptic history of Hurricane Irma

[Figure 1](#) shows the best track traces of both maximum sustained 10-m wind speed and minimum sea level pressure over the lifetime of Hurricane Irma. The easterly wave that spawned Hurricane Irma exited the African coast on 27 August 2017 ([Cangialosi et al. 2018](#)). As the disturbance gradually became better organized, tropical cyclogenesis was determined to occur around 0000 UTC 30 August. Six hours following the time of genesis, Irma reached tropical storm intensity and began to experience a period of RI, as the TC moved off to the west-northwest, across the eastern North Atlantic. Here, RI is defined following [Kaplan and DeMaria \(2003\)](#),

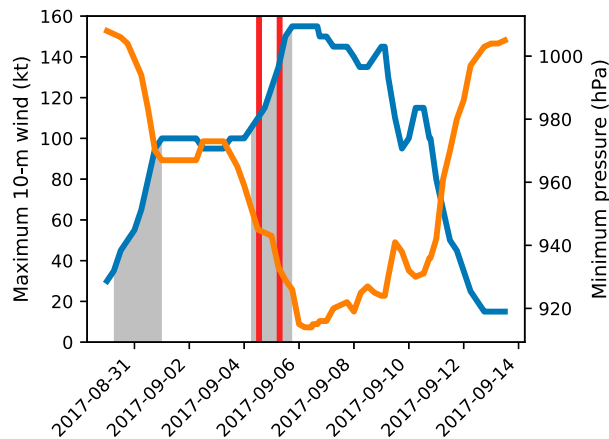


FIG. 1. Best track evolution of maximum sustained 10-m winds (kt; blue line) and minimum surface pressure (hPa; orange line) associated with Hurricane Irma (2017). Time periods associated with RI are shaded in gray. The red vertical lines depict the times of two ERC events.

which is equal to a 24-h increase in the maximum sustained 10-m wind  $\geq 30$  kt ( $1 \text{ kt} \approx 0.51 \text{ m s}^{-1}$ ). During this RI event, Irma intensified by 65 kt in only 42 h—as highlighted by the shaded region in Fig. 1—and reached major hurricane intensity. Following this period of RI, Hurricane Irma encountered a region of cooler sea surface temperatures (SSTs; Fig. 2) and the storm's intensity remained relatively steady for nearly 3 days. As the TC began to follow a more west-southwestward trajectory, Irma encountered increasing SSTs on 2 September (Fig. 2).

Beginning on 4 September 2017, Irma experienced a second RI period, intensifying to 155 kt by 1800 UTC 5 September (Fig. 1). The *initiation* of an RI event while a TC is at major hurricane intensity is a relatively rare event for storms in the North Atlantic basin, as Irma became the first TC to begin such an RI event since Hurricane Gilbert (1988), nearly 30 years earlier. Following Irma's second RI event, the TC tracked off to the west-northwest (Fig. 2), maintaining category 5 hurricane intensity on the Saffir–Simpson Hurricane Wind Scale for approximately 60 h, which is the second longest consecutive period on record in the North Atlantic basin (Cangialosi et al. 2018). The path of Irma brought the storm through the northeastern Caribbean islands, the Turks and Caicos, and the Bahamas, before making landfall in Cuba. Following landfall in Cuba, Irma began a turn to the northwest and then north, as the storm made additional landfalls in the Florida Keys and the Florida peninsula. In total, Hurricane Irma made seven landfalls, causing over 50 billion USD in damages and resulting in at least 47 direct deaths (Cangialosi et al. 2018).

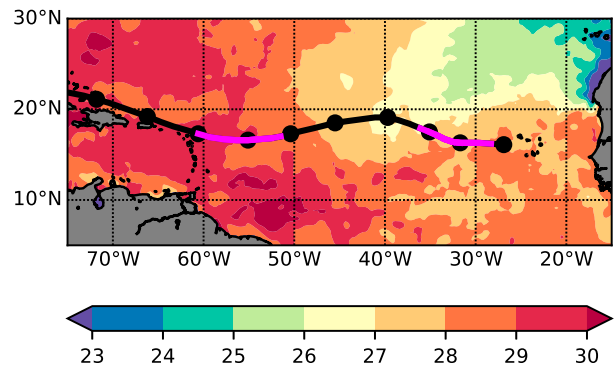


FIG. 2. Path of Hurricane Irma beginning at 0000 UTC 30 Aug 2017 (black line; black circles denote the position of the TC every 24 h) and SST ( $^{\circ}\text{C}$ ; shaded). RI periods are represented by the magenta lines.

The remainder of this study will seek to understand the characteristics associated with, and leading up to, Irma's second RI period, which occurred from 4 to 5 September (Fig. 1).

#### 4. Environmental influences on Irma's intensification

The evolution of the environmental vertical wind shear, moisture, SST, and ocean heat content leading up to, and during, Irma's second RI period are provided in Fig. 3. Here, the environmental conditions are obtained from analyses via the Statistical Hurricane Intensity Prediction Scheme (SHIPS; DeMaria and Kaplan 1994). For reference, Irma's intensity trace is provided in the dashed orange line. As seen in Fig. 3a, Hurricane Irma was located in an environment characterized by relatively favorable deep-layer (850–200 hPa) vertical wind shear magnitudes of less than  $5 \text{ m s}^{-1}$  at nearly every analysis time. The shear magnitudes are, generally, well below the climatological mean of all North Atlantic RI episodes of approximately  $5 \text{ m s}^{-1}$  (horizontal, red line in Fig. 3a). Early in Irma's lifetime, including the first RI period, the vertical shear direction was out of the northeast (Fig. 3b). Following the completion of the first RI event on 1 September 2017, the shear direction shifted to a southerly direction, before rotating anticyclonically back toward a northeasterly direction near the start of Irma's second period of RI on 4 September. Despite some oscillations, the vertical wind shear maintained a northerly component throughout Irma's second RI event.

Figures 3c and 3d demonstrate that although Irma was originally located in a relatively moist environment compared to the mean of North Atlantic RI episodes, Irma encountered a drier environment near the end of

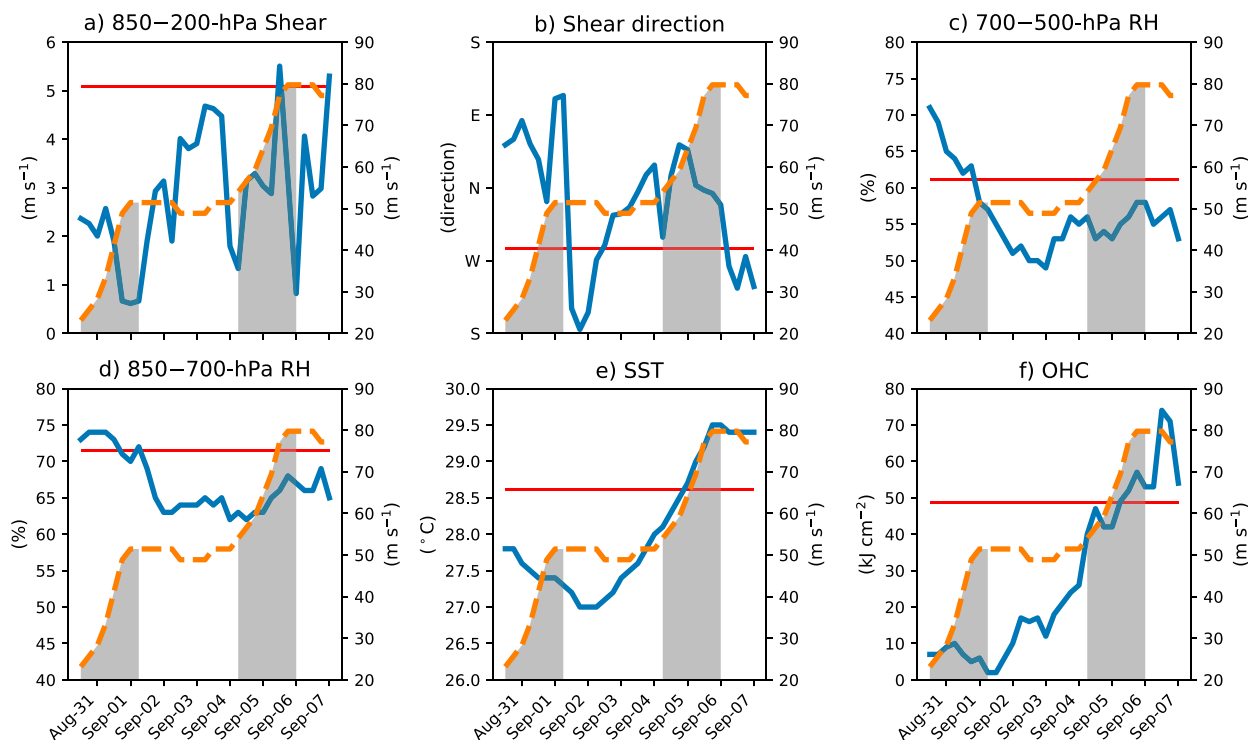


FIG. 3. SHIPS analyses (blue lines) of the (a) 850–200-hPa vertical wind shear magnitude ( $\text{m s}^{-1}$ ), (b) 850–200-hPa vertical wind shear direction (meteorological direction), (c) 700–500-hPa layer-averaged relative humidity (%), (d) 850–700-hPa layer-averaged relative humidity (%), (e) sea surface temperature ( $^{\circ}\text{C}$ ), and (f) maximum potential intensity ( $\text{m s}^{-1}$ ). Analyses span from 1200 UTC 30 Aug to 0000 UTC 7 Sep 2017. For a given parameter, the mean value for all RI episodes occurring from 1989 to 2017 are depicted by the horizontal red line. The intensity of Hurricane Irma ( $\text{m s}^{-1}$ ) is shown in the dashed, orange line.

the first RI period on 1 September, as measured by both 700–500-hPa (Fig. 3c) and 850–700-hPa relative humidity (Fig. 3d). The relative humidity in both layers maintained values 5%–10% less than the respective RI climatological means throughout Irma's second RI period. The unfavorable decrease in lower- and mid-tropospheric humidity during this time, however, was offset by an increase in SSTs (Fig. 3e) and ocean heat content (Fig. 3f), beginning on 2 September and continuing through 6 September. By the beginning of Irma's second RI event, SSTs had increased to  $28^{\circ}\text{C}$  and by the end of the RI event were near  $29.5^{\circ}\text{C}$ , which is well above the climatological mean for North Atlantic RI episodes (Fig. 3e). Ocean heat content displayed a particularly sharp increase in the 12–24 h preceding Irma's second RI event, increasing from  $<20 \text{ kJ cm}^{-2}$  to nearly  $50 \text{ kJ cm}^{-2}$  from 3 September to 4 September.

These results suggest Irma's intensity evolution was closely linked to changes in the environment. Irma's first RI period occurred in a low shear and relatively moist environment, despite being over marginal SSTs and low ocean heat content. As Irma traversed over cooler SSTs and into a drier environment, the TC experienced a

plateau in intensity for approximately 3 days. It was not until SSTs and ocean heat content increased toward levels more typically associated with North Atlantic RI episodes that Irma underwent a second period of RI, before reaching its peak intensity.

Despite the strong relationship between the evolution of Irma's intensity and its environment, it is important to understand the response of the convective and TC vortex structures during this time, as these features are what ultimately dictate the rate of TC intensity change.

### 5. Vortex evolution during RI

Irma's second RI period was well-sampled by multiple aircraft reconnaissance missions, as seen by the flight paths of the Air Force WC-130 and NOAA P3 missions analyzed in this study (Fig. 4). NOAA P3 missions began sampling the core of Hurricane Irma around 2100 UTC 3 September, with subsequent missions flown every 12 h. Air Force missions were also conducted every 12 h, beginning on 4 September, with center-fix times staggered between the P3 fix times. Consequently, the inner core of Irma was sampled at a frequency of at least once every



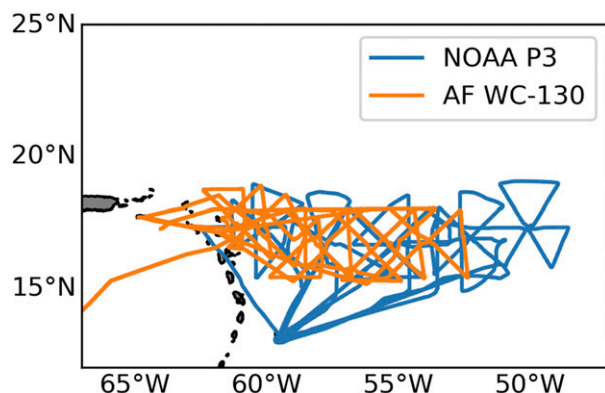


FIG. 4. Flight patterns of all NOAA WP-3D (blue) and Air Force WC-130 (orange) aircraft reconnaissance missions analyzed within this study.

6 h, beginning around 0900 UTC 4 September, near the start of the second RI event.

The evolution of the storm-relative, azimuthally averaged, tangential wind ( $\bar{V}_T$ ) at flight level from each aircraft reconnaissance mission flown into Irma is shown in Fig. 5. Here, azimuthally averaged velocities are calculated for each individual center fix, using both the inbound and outbound legs. By using the mean of a single pass through the storm, rather than the mean of all legs for a given mission, a greater temporal resolution of the vortex structure was obtained during a period where both the intensity and structure of the vortex were rapidly evolving (Fig. 5). Although such a technique can yield noisier analyses due to potential vortex asymmetries, manual inspection of the radial flight legs revealed the symmetric component of the vortex largely outweighed any asymmetries. The flight-level altitude displayed some small variability, as the NOAA P3 missions made center fixes at an altitude of either 750 or 700 hPa, while the Air Force WC-130 consistently made fixes at 700 hPa. The evolution of  $\bar{V}_T$  presented in Fig. 5 does not appear particularly sensitive to the variability in flight-level altitude within this study. It should also be noted that Fig. 5 was constructed relative to a TC center that maximized  $\bar{V}_T$  within a 5-km annulus, centered on the radius of maximum wind (RMW). The recentering technique used here allows for the possibility that the TC center does not exist directly on the flight track, potentially due to differences in the storm-relative (used here) and Earth-relative (used operationally) frameworks.

From Fig. 5, it is apparent that the maximum  $\bar{V}_T$  increases throughout the majority of the times shown, consistent with the RI period in the best track observations; however, the RMW (depicted by the black, dashed line) experiences two particularly rapid outward

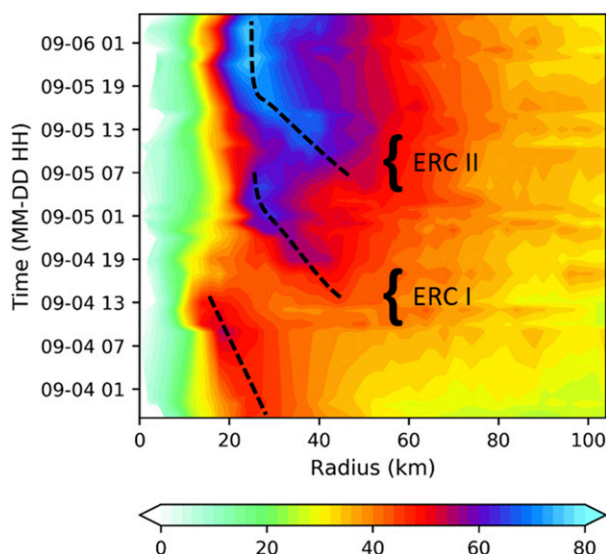


FIG. 5. Time series of azimuthally averaged tangential wind ( $\bar{V}_T$ ;  $\text{m s}^{-1}$ ) measured at flight-level as observed by both NOAA P3 and Air Force WC-130 aircraft. Black dashed lines subjectively identify the eyewall location. The two eyewall replacement cycles are indicated by ERC I and ERC II.

pulses, before contracting slowly inward. The first such outward pulse occurs between 1200 and 1800 UTC 4 September, where the RMW grows from nearly 15 to 45 km. The second outward pulse in the RMW occurs between 0600 and 0900 UTC 5 September, where the RMW grows from approximately 25 to 45 km. The evolution of both of these radially outward pulses of  $\bar{V}_T$ , as well as their subsequent contraction, are consistent with ERCs (Sitkowski et al. 2011). Hereafter, the first outward pulse in the RMW will be referred to as ERC I, while the second outward pulse will be referred to as ERC II, as indicated in Fig. 5.

The rate at which both ERCs complete is unusually rapid. In a climatological study of ERCs using flight-level aircraft reconnaissance observations, Sitkowski et al. (2011) determined that a typical ERC takes 36 h to complete. In the case of Irma, the secondary  $\bar{V}_T$  maximum leading up to ERC I wasn't observed until approximately 0900 UTC 4 September, with the inner  $\bar{V}_T$  maximum dissipating by 1900 UTC—a period of only 10 h. ERC II occurred just as rapidly, with the outer  $\bar{V}_T$  maximum first appearing around 0400 UTC 5 September and the inner  $\bar{V}_T$  maximum disappearing by 1300 UTC, totaling a remarkably quick 9-h period. The radial locations of the primary and secondary  $\bar{V}_T$  maxima during the ERCs were also uncommon. For example, Sitkowski et al. (2011) found that the primary and secondary wind maxima at the start of ERC events are 35 and 106 km, respectively. Here, the secondary  $\bar{V}_T$  maxima form at radii less than half the climatological mean in both

## 85–91-GHz PCT (K)

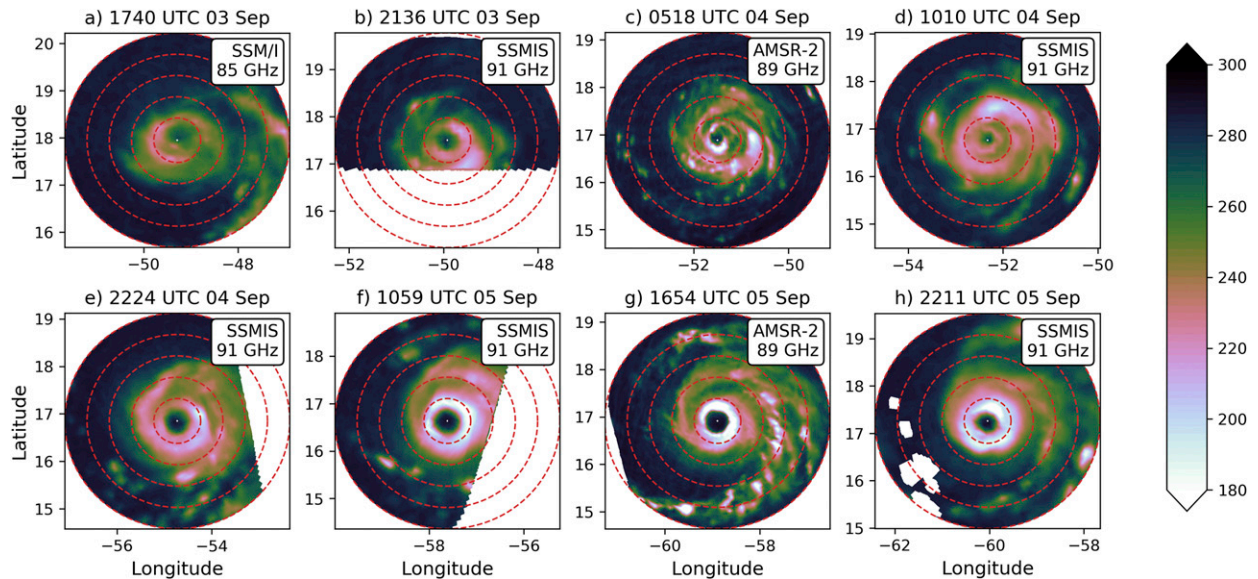


FIG. 6. Storm-centered microwave overpasses displaying 85–91-GHz polarization corrected brightness temperatures (PCT; K; shaded) associated with Hurricane Irma. Red dashed radial-rings are spaced in 50-km increments. The overpasses occurred at (a) 1740 UTC 3 Sep, (b) 2136 UTC 3 Sep, (c) 0518 UTC 4 Sep, (d) 1010 UTC 4 Sep, (e) 2224 UTC 4 Sep, (f) 1059 UTC 5 Sep, (g) 1654 UTC 5 Sep, and (h) 2211 UTC 5 Sep 2017. The sensor and observing frequency of each overpass are given in the top-right corner of each panel.

ERCs. Additionally, the radial displacements between the primary and secondary  $\bar{V}_T$  maxima in both ERC I and ERC II are initially around 25–30 km, significantly smaller than the climatological value of 71 km.

The two ERCs noted in Fig. 5 are consistent with the convective evolution observed by passive microwave satellite imagery, shown in Fig. 6, which depicts storm-centered 85–91-GHz brightness temperatures from multiple sensors between 3 and 5 September. The 85–91-GHz band is particularly sensitive to frozen hydrometeors, with depressed brightness temperatures indicating a greater amount of “ice scattering,” and hence, increased deep-convective activity.

Prior to the onset of RI, at 1740 UTC 3 September, Hurricane Irma displayed a ring of 85–91-GHz polarization-corrected brightness temperatures  $<250$  K associated with the eyewall of the storm (Fig. 6a). Over the next 12 h, minimum brightness temperatures decreased and the eyewall contracted (Figs. 6a–c). Additionally, a convective band formed on the south side of the storm, which was downshear of the TC center according to SHIPS analyses (Fig. 3b). The presence of the downshear convective band is consistent with multiple previous studies that have found TC rainband activity occurs preferentially in the downshear part of the TC circulation (e.g., Willoughby et al. 1984; Corbosiero and Molinari 2002; Houze 2010; Hense and Houze 2012;

Didlake and Houze 2013a). The azimuthal extent of the convective band on the south side of Irma increased with time, such that the rainband completely enclosed the eyewall by 1010 UTC 4 September (Fig. 6d). This time nearly coincides with the first observance of an outer  $\bar{V}_T$  maximum leading up to ERC I, as measured by aircraft reconnaissance (Fig. 5).

By the time of the next available overpass at 2224 UTC 4 September, the size of the eye had increased, with a single eyewall present (Fig. 6e). Such a convective evolution is consistent with previous ERC analyses (Black and Willoughby 1992; Kossin and Sitkowski 2009; Sitkowski et al. 2011; Didlake et al. 2018) and agrees with the larger RMW at flight-level shown in Fig. 5. In addition to the completion of ERC I, new convective bands developed on the northwest and southeast sides of the TC center (Fig. 6e). Because this time was only about 6 h prior to the first appearance of the secondary wind maximum associated with ERC II (Fig. 5), it is possible these convective bands were associated with secondary eyewall formation in ERC II; however, the relatively poor temporal resolution of microwave observations precludes a clear linkage. The following microwave overpass at 1059 UTC 5 September, over 12 h later and near the end of ERC II, revealed a nearly symmetric ring of PCT  $<200$  K, indicative of intense convection (e.g., Mohr and Zipser 1996a,b; Mohr et al. 1996; Cecil and Zipser 1999). By the end of

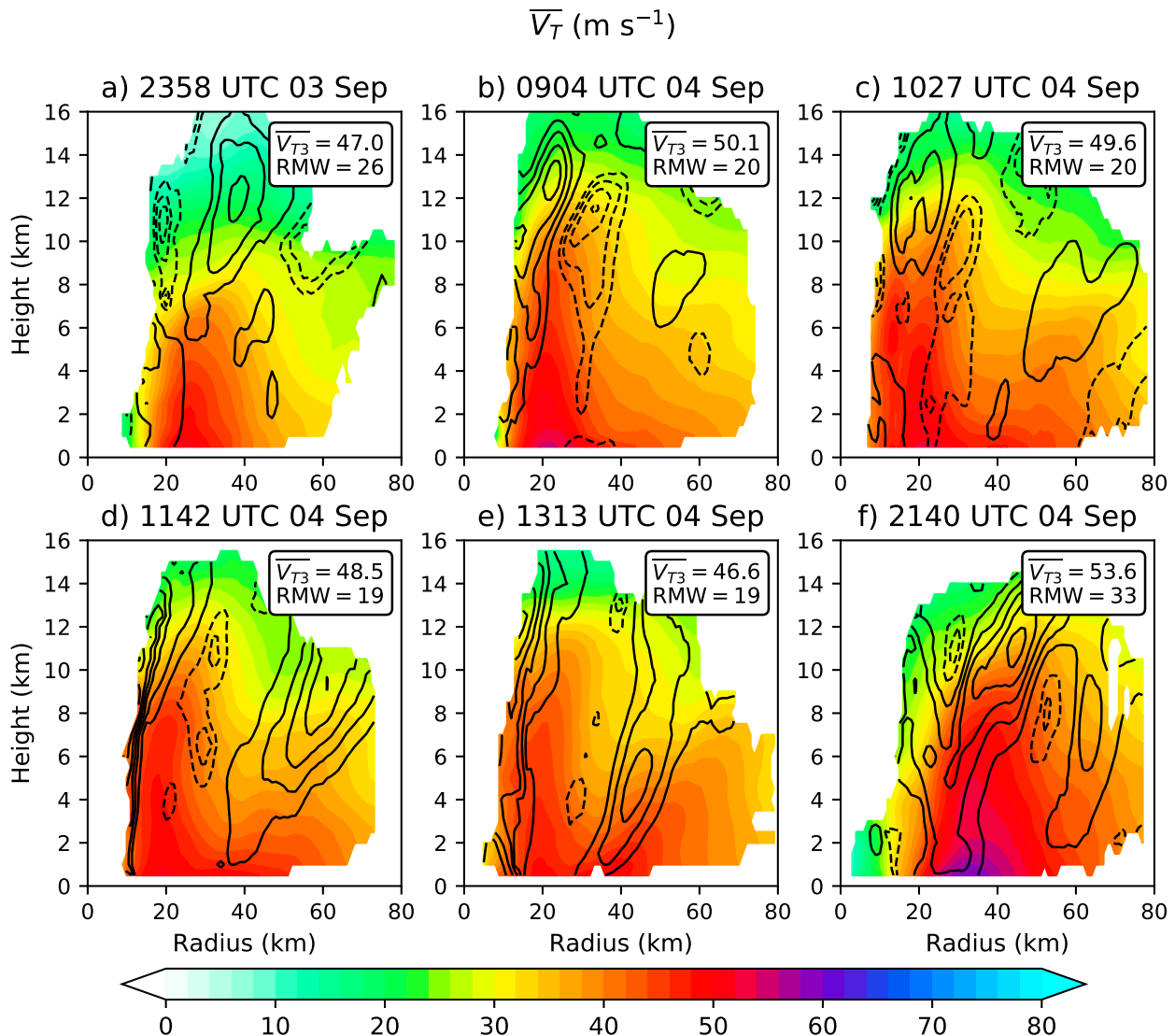


FIG. 7. Azimuthally averaged tangential wind ( $\overline{V_T}$ ; m s<sup>-1</sup>; shaded) and vertical velocity (contours) obtained from (a) the 2358 UTC 3 Sep center pass. Positive vertical velocity values are shown in the solid contours every 0.5 m s<sup>-1</sup>, while negative vertical velocity values are shown in the dashed contours every 0.2 m s<sup>-1</sup>. The inset of the panel depicts the magnitude of the maximum azimuthally averaged tangential wind at a height of 3 km ( $\overline{V_{T3}}$ ; m s<sup>-1</sup>) and the radius of  $\overline{V_{T3}}$  (RMW; km). (b) As in (a), but for the 0904 UTC 4 Sep center pass. (c) As in (a), but for the 1027 UTC 4 Sep center pass. (d) As in (a), but for the 1142 UTC 4 Sep center pass. (e) As in (a), but for the 1313 UTC 4 Sep center pass. (f) As in (a), but for the 2140 UTC 4 Sep center pass. For each flight, only radii with at least 33% azimuthal coverage are shown.

the RI period, minimum PCT continued to decrease to temperatures <180 K within a single, vigorous eyewall (Figs. 6g,h).

To understand how the three-dimensional TC vortex structure evolved during ERC I and ERC II, the following subsections will examine TDR observations from multiple P3 flights.

#### a. The evolution of ERC I

The development of the outer eyewall, as well as the completion of ERC I, can be viewed in the form of

azimuthally averaged, radius–height sections of tangential wind and vertical velocity, as seen in Fig. 7. In this case, each panel displays the azimuthally averaged values for a given center pass. Beginning with the last pass of the 170903H1 flight, Fig. 7a displays the structure of Hurricane Irma prior to secondary eyewall formation, at 2358 UTC 3 September. At this time, a single, well-defined eyewall exists, with a RMW of 26 km at a height of 3 km and sloping outward to approximately 40 km at an altitude of 10 km. Just inside the RMW, azimuthally averaged ascent >0.5 m s<sup>-1</sup> exists throughout much of



the troposphere, with maximum azimuthally averaged ascent  $>1.5 \text{ m s}^{-1}$  at a height of 12 km.

By the time of the first center pass of the 170904H1 mission at 0904 UTC 4 September, the TC vortex had intensified throughout the troposphere (Fig. 7b), consistent with the onset of RI in the best track beginning at 0600 UTC 4 September (Fig. 1). The RMW had contracted to a radius of 20 km at a height of 3 km, with the main eyewall ascent also shifting radially inward, remaining inward of the RMW. The first appearance of a secondary wind maximum was also observed around this time, indicated by an outward sloping local maximum in  $\bar{V}_T$  beginning at a radius of approximately 50 km in the lowest 4 km of the troposphere, in agreement with the flight-level observations shown in Fig. 5. A region of ascent  $>0.5 \text{ m s}^{-1}$  was observed near the secondary wind maximum, at a height of 6–8 km (Fig. 7b). Additionally, a deep layer of subsidence  $< -0.2 \text{ m s}^{-1}$  was situated between the primary and developing secondary eyewalls. Such a ring of subsidence is consistent with a moat region that frequently develops between the primary and secondary eyewalls during an ERC (Houze et al. 2007; Rozoff et al. 2008; Abarca and Corbosiero 2011; Bell et al. 2012; Kepert 2013; Zhu et al. 2015; Tyner et al. 2018).

During the next three passes, the secondary  $\bar{V}_T$  maximum became progressively better defined, while the maximum values of  $\bar{V}_T$  associated with the primary eyewall slightly decreased, particularly in the lowest 2–3 km of the troposphere (Figs. 7c–e). Ascent in the developing secondary eyewall also experienced a shift from being maximized in the midtroposphere, between 7 and 10 km (Figs. 7b–d), to becoming more bottom-heavy, with peak ascent between 4 and 6 km by 1313 UTC 4 September (Fig. 7e). At each time shown, ascent associated with the secondary eyewall was located radially inward of the secondary  $\bar{V}_T$  maximum. Such a convective configuration would favor the spinup of the outer eyewall by advecting larger angular momentum surfaces inward (Shapiro and Willoughby 1982; Montgomery and Smith 2014; Smith and Montgomery 2016).

During the next mission, at 2140 UTC 4 September, a pronounced, double  $\bar{V}_T$  structure was no longer evident, indicating the completion of ERC I (Fig. 7f). Instead a single, more intense  $\bar{V}_T$  maximum was observed at a radius of 30–35 km; much larger than the RMW at the start of ERC I. Following suit, the maximum azimuthally averaged ascent had also advected inward and was still located radially inward of the RMW. A new, secondary ascent maximum was also observed at this time, located at a radius of 60 km. Although no clear-cut secondary  $\bar{V}_T$  maximum accompanied the local ascent maximum, a broadening of the  $\bar{V}_T$  field was observed compared to earlier passes, with some hints of a weak,

secondary  $\bar{V}_T$  maximum at a height of 4–8 km. It will be shown later that the new secondary ascent maximum appearing in Fig. 7f can be linked to the onset of ERC II.

A view of the azimuthally averaged radial flow ( $\bar{V}_R$ ) within Hurricane Irma during ERC I, matching the times shown in Fig. 7, is provided in Fig. 8. Prior to the onset of ERC I, Irma's inner core was characterized by weak inflow throughout the majority of the region below 6 km (Fig. 8a). Above 6 km, outflow was focused within two main channels; the first outflow channel coincided with the top of the primary eyewall and extended to heights  $>14$  km, while the second outflow channel was focused between 6 and 10 km in height, extending radially outward from the primary eyewall. The development of the secondary eyewall occurred along the leading edge of a descending region of inflow between 2 and 6 km in height within an approximate 40–80-km radial band (Fig. 8b). Directly above the descending inflow jet was a local outflow maximum, which displayed acceleration near the region of midlevel ascent associated with the developing secondary eyewall. This descending inflow and overturning circulation near the location of SEF resembles the observational analysis of an SEF event in Hurricane Earl (2010) by Didlake et al. (2018), although Didlake et al. (2018) determined the descending inflow jet was an asymmetric feature. Here, potential asymmetries will be examined in section 6.

Over the next three passes, the overturning circulation associated with the developing secondary eyewall progressively reached farther down, toward the surface (Figs. 8c–e). At the same time, boundary layer inflow that was originally feeding the primary eyewall became progressively weaker, until the inner eyewall began to collapse, with outflow noted throughout the lowest 2 km near the primary eyewall (Fig. 8e). Following the completion of ERC I, a more vigorous inflow layer became established, with structures consistent with previous observational studies of supergradient flow in the boundary layer (e.g., Montgomery et al. 2014b; Rogers et al. 2015; Abarca et al. 2016), as a region of outflow was located near the RMW, directly above the inflow region, between a height of 1–2.5 km (Fig. 8f). A secondary overturning circulation was observed above the boundary layer corner-flow region, characterized by inflow between approximately 3–7 km and outflow above 7 km, although these structures slanted upward with increasing radius. Consistent with the hypotheses of Smith et al. (2009), the midlevel inflow seen in Irma at this time was related to a broadening of the TC vortex (Fig. 7f), as relatively large angular momentum surfaces are advected inward above the boundary layer.

Despite the rapid completion of ERC I, the evolution of the TC vortex during the ERC displayed many

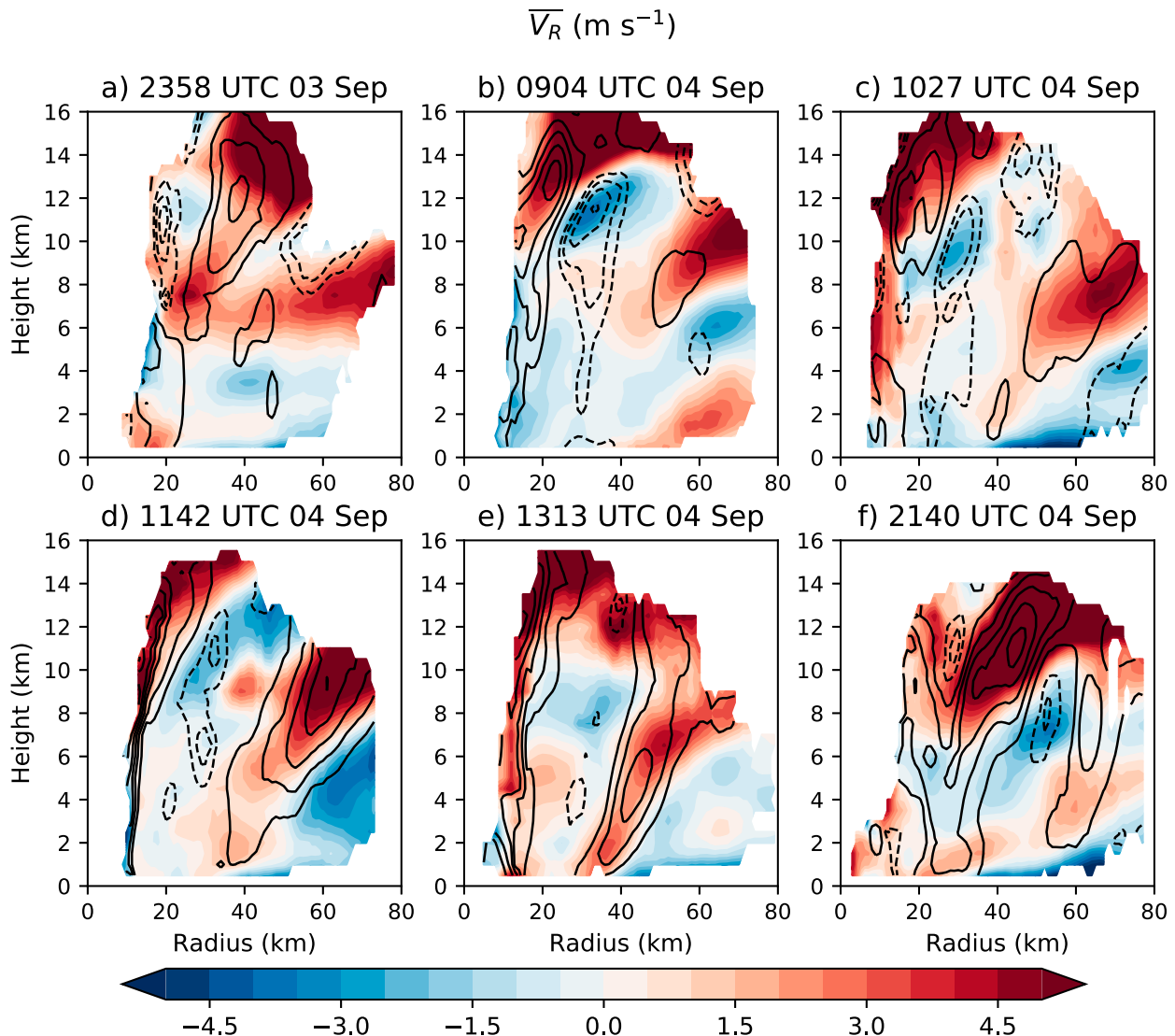


FIG. 8. Azimuthally averaged radial wind ( $\overline{V_R}$ ;  $\text{m s}^{-1}$ ; shaded) and vertical velocity (contours) obtained from (a) the 2358 UTC 3 Sep center pass. Positive vertical velocity values are shown in the solid contours every  $0.5 \text{ m s}^{-1}$ , while negative vertical velocity values are shown in the dashed contours every  $0.2 \text{ m s}^{-1}$ . (b) As in (a), but for the 0904 UTC 4 Sep center pass. (c) As in (a), but for the 1027 UTC 4 Sep center pass. (d) As in (a), but for the 1142 UTC 4 Sep center pass. (e) As in (a), but for the 1313 UTC 4 Sep center pass. (f) As in (a), but for the 2140 UTC 4 Sep center pass. For each flight, only radii with at least 33% azimuthal coverage are shown.

similarities to the canonical ERC described in the literature (e.g., Sitkowski et al. 2011). Namely, an outer eyewall developed at a radial distance of 2–3 times the RMW, while a moat of subsidence formed between the eyewalls. With time, ascent in the inner eyewall weakened, followed by the total collapse of the inner eyewall, which was associated with a brief weakening of the maximum  $\overline{V_T}$ .

#### b. The evolution of ERC II

The evolution of  $\overline{V_T}$ , as well as azimuthally averaged vertical velocities, during ERC II are shown in Fig. 9.

The vortex structure at 2307 UTC 4 September is shown in Fig. 9a, which was the subsequent center pass following Figs. 7f and 8f. Compared to the previous pass through the storm, maximum  $\overline{V_T}$  had increased by approximately  $1\text{--}2 \text{ m s}^{-1}$  in the lowest 5 km, while the 3-km RMW had contracted to 31 km (Fig. 9a). Additionally, the secondary ascent maximum had contracted inward, now located within a 40–60 km radial band. Over the final two passes of the flight, the secondary ascent maximum continued to advance radially inward as peak  $\overline{V_T}$  values continued to increase (Figs. 9b,c). Additionally, although no clear secondary  $\overline{V_T}$  maximum was observed,

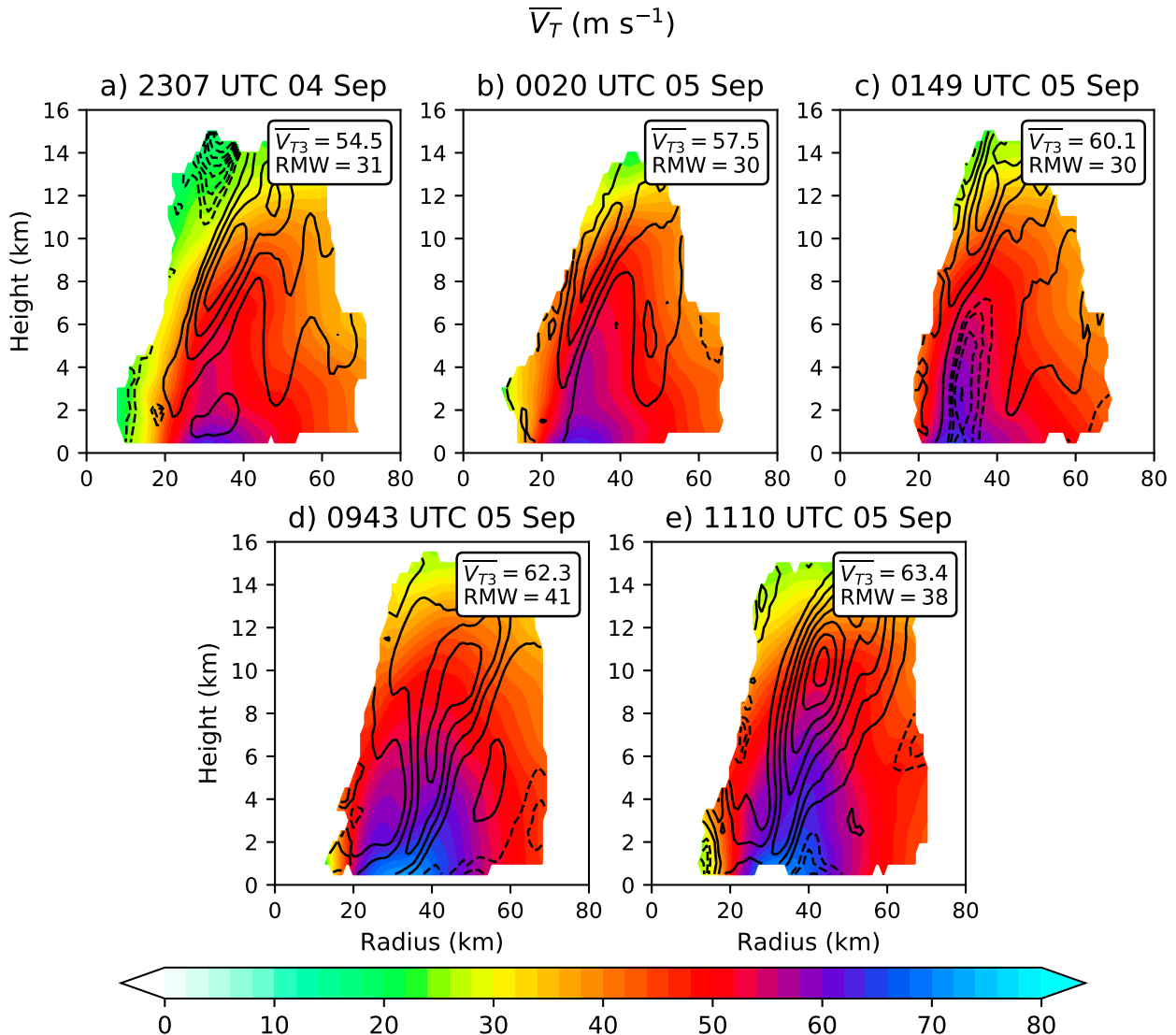


FIG. 9. As in Fig. 7, but for (a) the 2307 UTC 4 Sep pass, (b) the 0020 UTC 5 Sep center pass, (c) the 0149 UTC 5 Sep pass, (d) the 0943 UTC 5 Sep center pass, and (e) the 1110 UTC 5 Sep center pass.

a broadening of the TC vortex occurred during this period, especially in the lowest 3 km, where  $\overline{V_T}$  contours flared outward near the location of the secondary ascent maximum. The final pass of the mission at 0149 UTC 5 September, detected a band of subsidence between the two ascent maxima, near the location of the  $\overline{V_T}$  maximum (Fig. 9c). The band of subsidence resembles a moat region and may have signaled the subsequent ERC, although radar reflectivities at this time did not show signs of a ring of lower reflectivities (not shown).

The following pass through Irma 8 h later revealed a fairly complex vortex structure (Fig. 9d). Double  $\overline{V_T}$  maxima were observed between 2 and 5 km in height, with the inner and outer maxima located at radii of approximately 25 and 41 km, respectively. Interestingly,

the double  $\overline{V_T}$  maxima appeared rooted together to a single  $\overline{V_T}$  maximum within the TC boundary layer, while a single  $\overline{V_T}$  maximum was observed above a height of 5 km. The vertical velocity structure had also significantly changed, as the outward ascent maximum had contracted to a radius inward of 40 km in the lowest 4 km of the troposphere with appreciably larger maximum ascent values, peaking at  $>2 \text{ m s}^{-1}$ . Conversely, the inner ascent maximum experienced a significant weakening, particularly in the lower troposphere, with ascent values  $>0.5 \text{ m s}^{-1}$  confined to heights above 6 km. Although uncommon, the structure of the TC vortex at this time closely resembles a large-eddy simulation of an intense ( $\overline{V_T} > 70 \text{ m s}^{-1}$ ) TC performed by Stern and Bryan (2018), which also featured midtropospheric

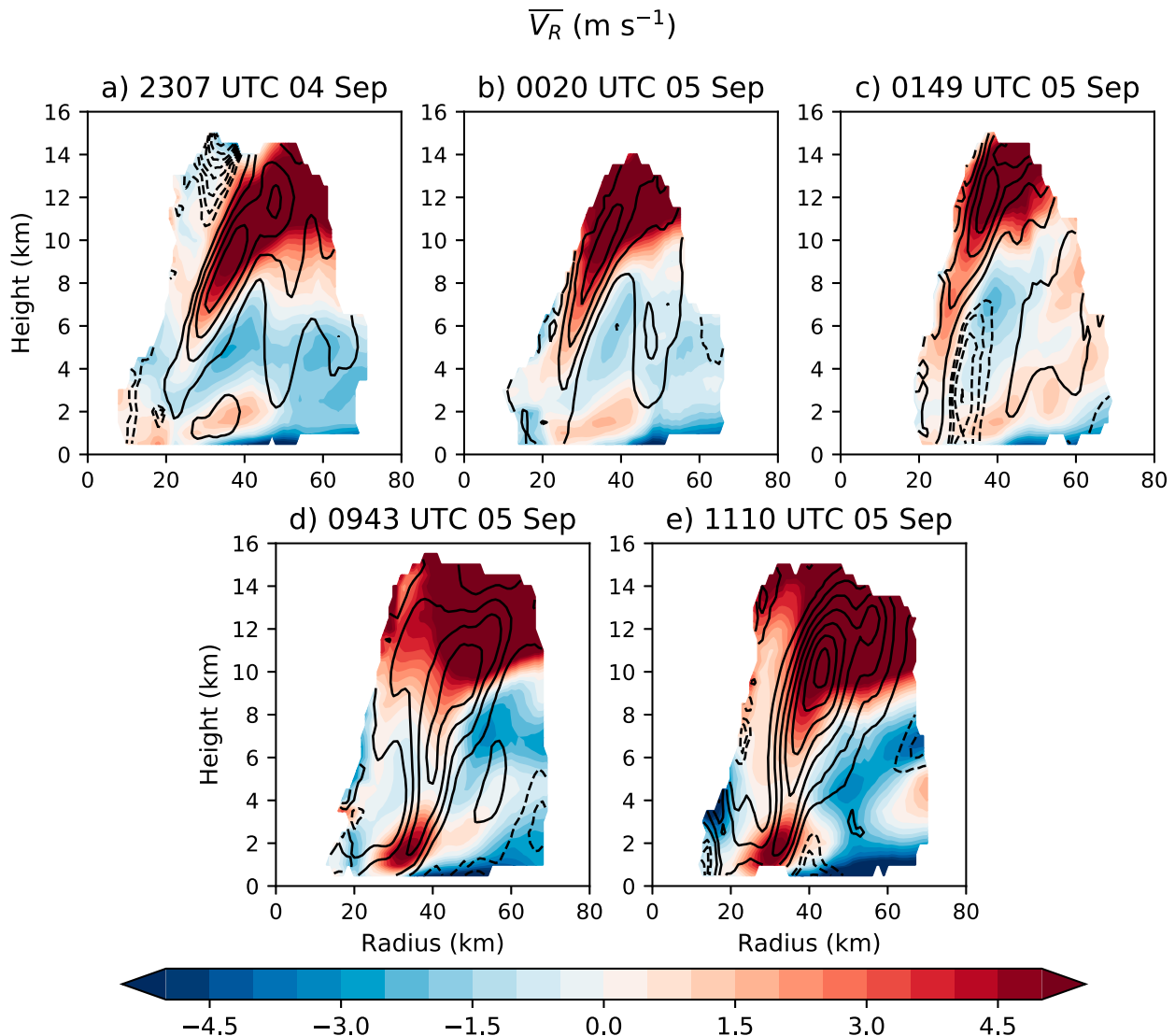


FIG. 10. As in Fig. 8, but for (a) the 2307 UTC 4 Sep pass, (b) the 0020 UTC 5 Sep center pass, (c) the 0149 UTC 5 Sep pass, (d) the 0943 UTC 5 Sep center pass, and (e) the 1110 UTC 5 Sep center pass.

double  $\overline{V}_T$  maxima, joined together within the boundary layer (see their Fig. 1b).

The double  $\overline{V}_T$  maxima structure disappeared over the following 1–2 h, as a single  $\overline{V}_T$  maximum was observed throughout the troposphere by 1110 UTC 5 September, signaling the completion of ERC II (Fig. 9e). The double ascent maxima vanished while maximum ascent values continued to increase to values  $>3.5 \text{ m s}^{-1}$ .

The evolution of  $\overline{V}_R$  during ERC II is provided in Fig. 10. Prior to the development of the secondary  $\overline{V}_T$  maximum, the  $\overline{V}_R$  field resembled Fig. 8f, with two primary regions of inflow feeding the primary eyewall (Figs. 10a–c). The boundary layer and midtropospheric inflow regions were separated by outflow at an altitude

between approximately 1–3 km, again resembling a corner-flow region associated with supergradient flow (Smith et al. 2009; Smith and Montgomery 2015, 2016). The terminus of the outflow component of the corner-flow region was met by a deeper layer of inflow near a radius of 50–60 km (Figs. 10a–c). This convergent region was coincident with the base of the secondary azimuthally averaged ascent maximum, which contracted inward with time and preceded the formation of the secondary  $\overline{V}_T$  maximum.

At the time of the next pass through the TC 8 h later, a large increase in  $\overline{V}_R$  was observed in the lowest 3 km of the troposphere, within the corner-flow region (Fig. 10d). The majority of the outflow became concentrated within a 25–40 km radial band, with a



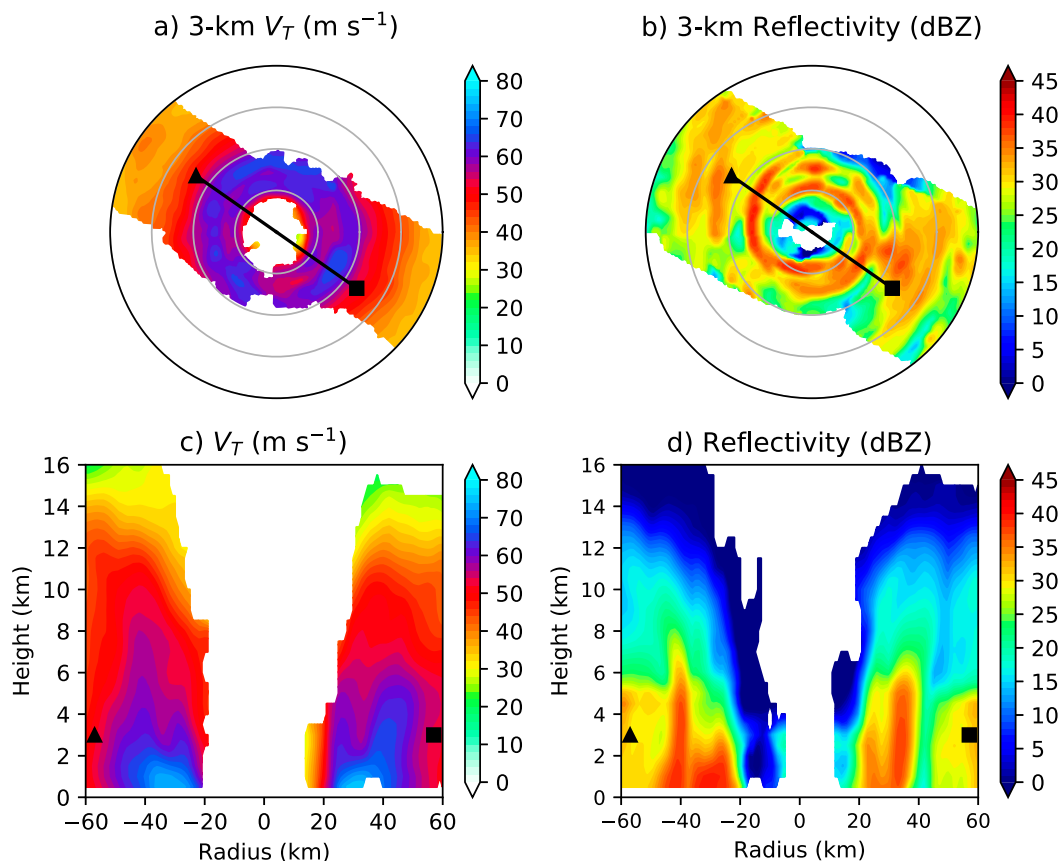


FIG. 11. (a) Plan view of 3-km tangential velocity ( $\text{m s}^{-1}$ ) obtained from the 0943 UTC 5 Sep center pass. Gray radial rings are spaced in 25-km increments. (b) As in (a), but for radar reflectivity (dBZ). (c) A northwest–southeast vertical cross section of tangential velocity ( $\text{m s}^{-1}$ ) taken along the black line shown in (a). For perspective, the black triangle and square markers are shown. (d) As in (c), but for radar reflectivity (dBZ).

shallow—but intense—inflow layer located underneath. Less midtropospheric inflow was noted near the location of the inner eyewall, with the bulk of the inflow terminating near a radius of 40 km, very near the location of the outer  $\bar{V}_T$  maximum (Figs. 9d, 10d). With less inflow feeding the inner eyewall, ascent within the inner eyewall began to decrease. Ultimately, the inner eyewall dissipated without any appreciable inflow to sustain it (Fig. 10e).

Despite the formation of a secondary eyewall and completion of ERC II, maximum  $\bar{V}_T$  values increased between every aircraft reconnaissance center pass shown in Fig. 9. This stands in contrast to ERC I, which was associated with a continuous decrease in maximum  $\bar{V}_T$  while the secondary eyewall became established (Fig. 7). It is possible that a brief weakening of the  $\bar{V}_T$  field occurred during the eight hour gap between the 0149 UTC 5 September and 0943 UTC 5 September center passes, although since the maximum  $\bar{V}_T$  increased by 2–3  $\text{m s}^{-1}$  between these passes, any temporary decrease was likely to be very short-lived (Fig. 9). An examination of

flight-level observations from an Air Force WC-130 mission (not shown) that sampled the storm during the aforementioned radar gap showed no robust signs of the TC vortex weakening, consistent with the flight-level winds shown in Fig. 5. As a result, it appears ERC II serves as the antithesis to the conceptual ERC model provided by Sitkowski et al. (2011), in which a TC experiences a period of weakening as the primary eyewall decays while the secondary eyewall intensifies. To some extent, Irma's vortex evolution during ERC II was reminiscent to that of Hurricane Isabel (2003), as a rapid expansion of the RMW in Isabel was observed near the end an RI event (Bell and Montgomery 2008).

The unique characteristics of ERC II, including the midtropospheric double  $\bar{V}_T$  maxima observed in Fig. 9c, motivate further analysis of the structure of the TC at this time. Figures 11a and 11b depict 3-km plan views of  $V_T$  as well as radar reflectivity, respectively, from the 0943 UTC 5 September pass through Hurricane Irma. In both panels, maxima in both  $V_T$  and reflectivity resemble an azimuthal wavenumber-2 pattern, with the

two bands of elevated values separated in radius by only 10–20 km. The bands of enhanced reflectivities are located 5–10 km closer toward the TC center than the bands of maximum  $V_T$ , consistent with the azimuthally averaged ascent being located within the RMW as shown in Figs. 9 and 10. Such a convective configuration agrees with composites of aircraft reconnaissance observations of intensifying tropical cyclones (Rogers et al. 2013).

Northwest–southeast vertical cross sections of both  $V_T$  and reflectivity are shown in Figs. 11c and 11d. Within the cross sections, a double eyewall structure is evident, with the outer eyewall featuring vertically deeper maxima in both  $V_T$  and reflectivity compared to the inner eyewall. The vertical cross sections indicate the lack of a pronounced moat at this time, as the two eyewalls appear to be in the process of merging together, particularly within the lowest 2 km of the troposphere. This result suggests the subsidence seen between the primary and secondary ascent maxima leading up to ERC II (Figs. 9c and 10c) may not have had sufficient time to generate a well-defined moat before the two eyewalls merged.

## 6. Potential mechanisms for secondary eyewall formation

### a. SEF I: Examination of a mesoscale descending inflow jet

To understand the causes of the different vortex evolutions during ERC I and ERC II, potential physical mechanisms that led to the two SEF events need to be examined. Recent work by Didlake et al. (2018), who also analyzed TDR observations of an SEF event, determined shear-induced convective asymmetries were responsible for SEF. In the case of Irma, however, the vertical wind shear magnitude was  $\leq 5 \text{ m s}^{-1}$  during both ERC periods (Fig. 3a), which is typically not strong enough to produce robust convective asymmetries, especially in major hurricanes (Chen et al. 2006). Nevertheless, passive microwave observations of Irma detected asymmetric convection within the rainband region of the storm, especially in the times leading up to ERC I (Figs. 6b,c). Recall that this rainband activity was the most vigorous in the downshear side of the storm (Fig. 3b), consistent with the expected convective configuration for a TC in a more moderate shear regime (Corbosiero and Molinari 2002; Chen et al. 2006; DeHart et al. 2014). This raises the question of whether SHIPS analyses potentially underestimated the shear magnitude during the times of SEF.

Previous work has demonstrated the magnitude and direction of the vertical wind shear displays sensitivity to

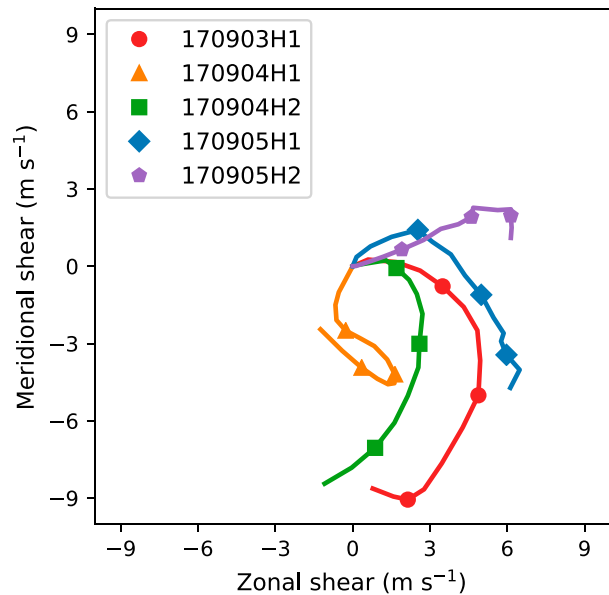


FIG. 12. Profiles of the 2–9 km local vertical wind shear ( $\text{m s}^{-1}$ ), relative to the mean flow at a height of 2 km, for flight 170903H1 (red circles), 170904H1 (orange triangles), 170904H2 (green squares), 170905H1 (blue diamonds), and 170905H2 (purple pentagons). Meridional shear values are displayed along the ordinate and zonal shear values displayed along the abscissa. Markers depict the 2–4, 2–6, and 2–8 km shear values. At each height, the profiles were computed using winds within 80 km of the TC center location.

the area over which it is computed (Riemer et al. 2010; Reasor and Eastin 2012; Reasor et al. 2013). To test for potential sensitivities between the vertical wind shear and the domain size, a local vertical wind shear was computed using TDR observations following the methods of Reasor and Eastin (2012) and Reasor et al. (2013). Figure 12 depicts the zonal and meridional components of the local shear profiles, relative to the mean flow at a height of  $2 \text{ km}^1$  for each P3 mission into Irma. In general, the 2–9-km local shear magnitudes were between  $5$  and  $9 \text{ m s}^{-1}$ , and thus, appreciably larger than the SHIPS analyses (Fig. 3a), which calculate shear using winds within a larger domain, that extends out to 500 km from the TC center. Additionally, the 2–9-km local shear directions were oriented  $0^\circ$ – $90^\circ$  to the left of the SHIPS shear direction. Active rainbands on the eastern side of Hurricane Irma on 5 September (Figs. 6f–h) are more consistent with the expected shear-relative convective structure obtained from the local shear

<sup>1</sup> The local shear was computed using winds within an 80-km radius relative to a TC center that was recalculated at every vertical level, following the same process described in section 2. Even so, the displacement between the TC center at the bottom and top of the 2–9-km shear layer was relatively small ( $<5 \text{ km}$ ) for each flight shown in Fig. 12.

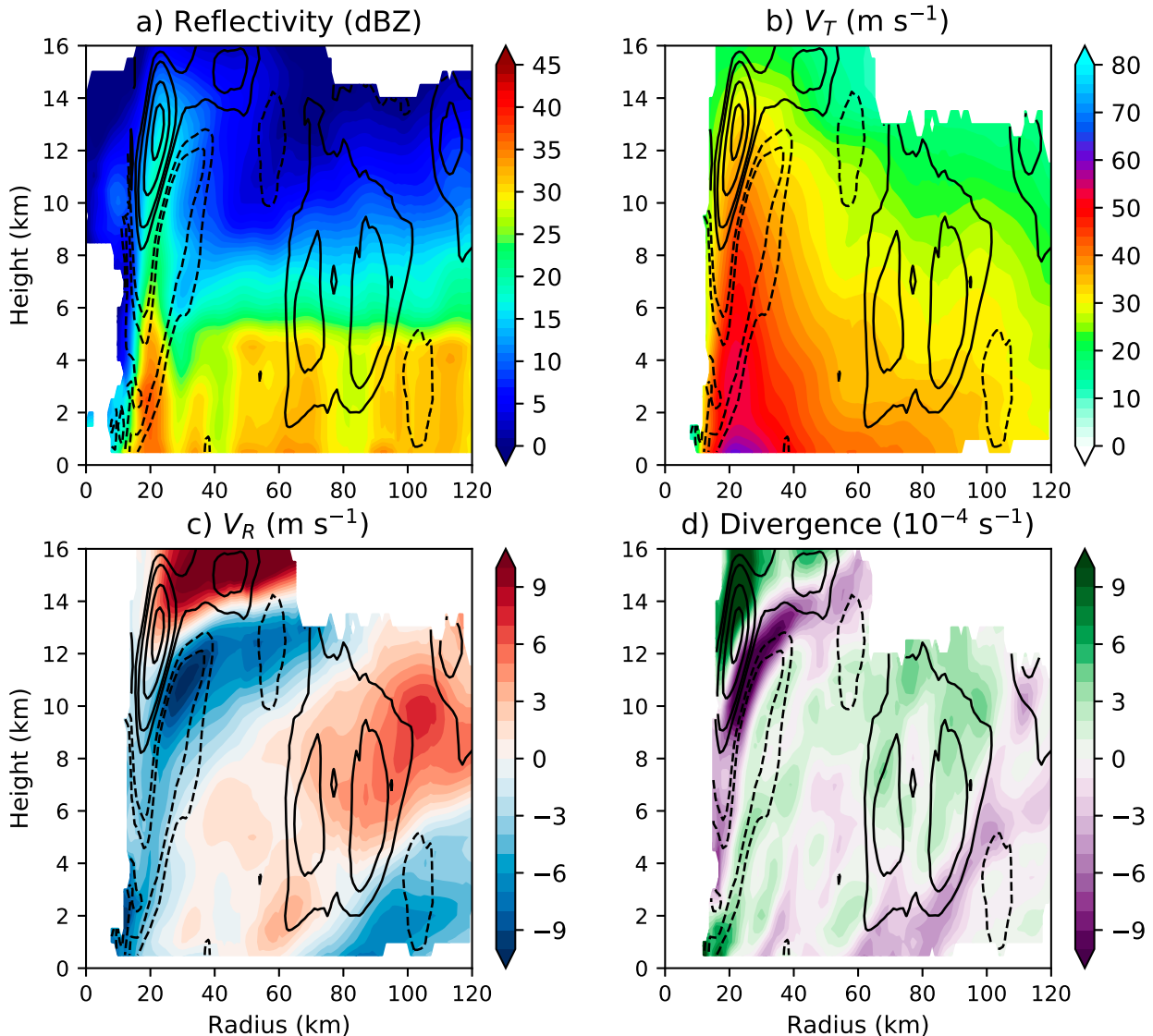


FIG. 13. (a) Azimuthally averaged values of radar reflectivity (dBZ; shaded) and vertical velocity (black contours) for the southeastern quadrant of the storm as sampled during the 0904 UTC 4 Sep pass. Positive vertical velocity values are drawn every  $0.5 \text{ m s}^{-1}$  between  $0.5$  and  $1.0 \text{ m s}^{-1}$  and every  $1.0 \text{ m s}^{-1}$  for values greater than  $1.0 \text{ m s}^{-1}$ . Negative values are dashed. (b) As in (a), but for tangential wind ( $V_T$ ; shaded;  $\text{m s}^{-1}$ ). (c) As in (a), but for radial wind ( $V_R$ ; shaded;  $\text{m s}^{-1}$ ). (d) As in (a), but for divergence (shaded;  $10^{-4} \text{ s}^{-1}$ ).

estimates, which comprised a larger, westerly zonal-shear component, compared to SHIPS shear analyses.

Utilizing the 2–9-km local shear direction computed from the TDR, the downshear-left quadrant of the TC was examined to ascertain whether the SEF mechanisms documented by [Didlake et al. \(2018\)](#) were also found in Irma's two SEF events. Figure 13 shows reflectivity,  $V_T$ ,  $V_R$ , and divergence averaged within the downshear-left quadrant during the 0904 UTC 4 September center pass, near the time of the first SEF event (SEF I). Unlike the azimuthally averaged values at this time (Figs. 7b and 8b), the downshear-left portion of the inner eyewall

displayed signs of weakening, with subsidence observed in the lowest 8 km of the troposphere, despite relatively large reflectivity values (Fig. 13a). Outward of this location, a broad, secondary ascent maximum was found within a 60–100-km radial band, with two smaller-scale ascent maxima embedded therein. Locations of locally greater ascent within the 60–100-km radial band were also associated with local maxima in  $V_T$  in the mid-troposphere. Similar to the findings of [Didlake et al. \(2018\)](#), the secondary ascent and  $V_T$  maxima were collocated with the inner edge of a mesoscale descending inflow jet (Fig. 13c) and a band of lower-tropospheric

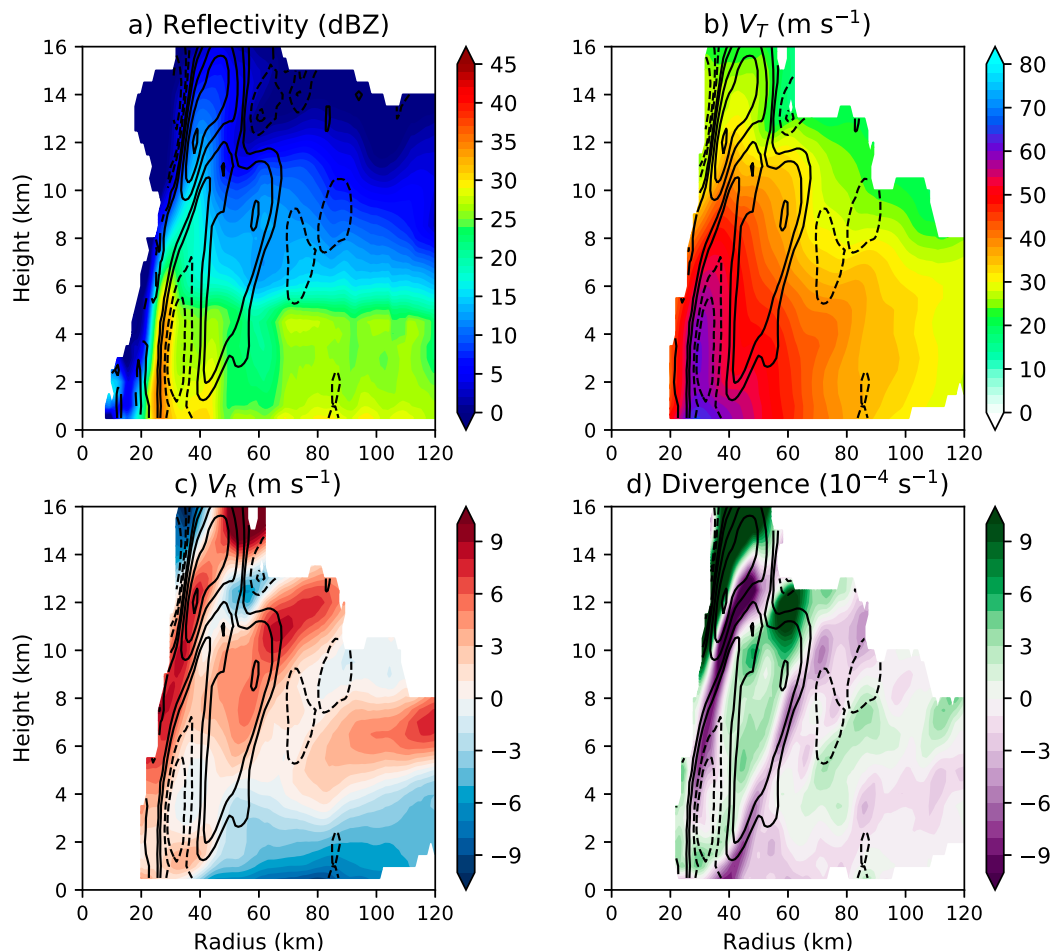


FIG. 14. As in Fig. 13, but for the 0149 UTC 5 Sep center pass.

convergence (Fig. 13d). Immediately above the leading edge of the inflow jet was a local maximum in outflow, indicative of a strengthening local secondary circulation and SEF, which was also seen in the SEF event examined by Didlake et al. (2018). Here, the formative secondary eyewall appeared to have acted as an inflow barrier to the primary eyewall, with minimal inflow between the primary and secondary eyewalls at heights between 0.5 and 8 km (Fig. 13c). Instead, the primary eyewall was linked to a secondary inflow jet existing above 10 km. The lack of lower-midtropospheric inflow associated with the primary eyewall likely explains the appearance of subsidence throughout this region, and signaled the upcoming demise of the primary eyewall during ERC I.

*b. SEF II: Consistency with unbalanced boundary layer processes*

Quadrant-averaged analyses of the downshear-left quadrant around the time of SEF prior to ERC II

(SEF II), shown in Fig. 14, reveal a different TC structure compared to SEF I. During SEF II, the TC inner-core structure was characterized by two primary ascent maxima, spaced only 20–30 km apart. An area of subsidence was observed between the ascent maxima, collocated with the  $V_T$  maximum (Fig. 14b). A secondary  $V_T$  maximum was observed at the base of the outer ascent maximum, between heights of 1–3 km, but sloped radially outward above a height of 3 km. Unlike the  $V_R$  structure seen in SEF I, the  $V_R$  field associated with SEF II did not feature a prominent descending inflow jet (Fig. 14c). Instead, the lower-tropospheric inflow layer abruptly slowed at the interface of a local maximum in outflow associated with an apparent corner-flow region, similar to the azimuthally averaged analyses in Figs. 10a–c. A convergent boundary was observed at the interface of the inflow layer and corner-flow region, which fueled ascent into the formative outer eyewall (Fig. 14d). The secondary ascent maximum was also linked to a local overturning circulation, with a local maximum in outflow





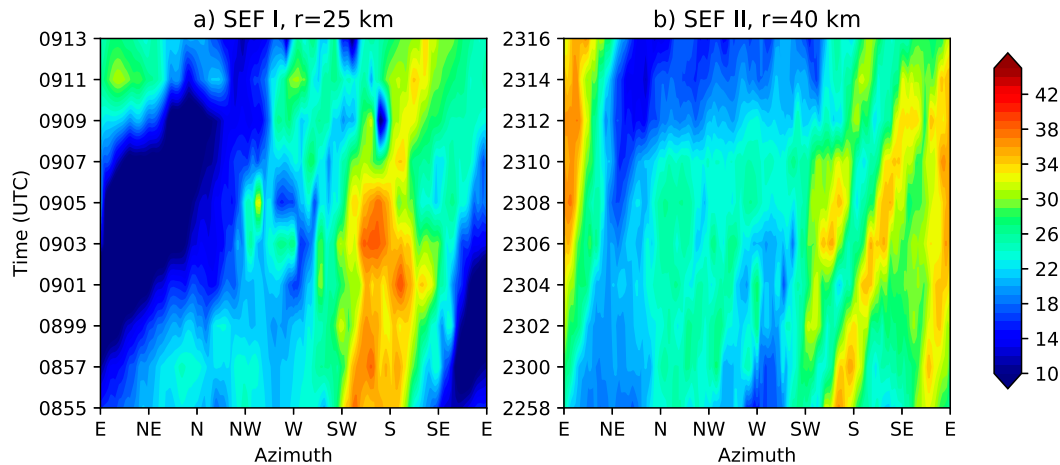


FIG. 16. (a) Time–azimuth diagram of LFR composite reflectivity (dBZ) observed during the 0904 UTC 4 Sep center pass, near the time of SEF I. Values are shown for a radius of 25 km from the TC center, corresponding to the dashed magenta line seen in Fig. 15c. (b) Time–azimuth diagram of LFR composite reflectivity (dBZ) observed during the 2307 UTC 4 Sep center pass, near the time of SEF II. Values are shown for a radius of 40 km from the TC center, corresponding to the dashed magenta line seen in Fig. 15f. In both panels, radar sweeps of reflectivity were averaged over a two-minute period centered along the time displayed on the ordinate of the diagram.

of the eyewall, terminating at radii of 40–50 km from the TC center (Fig. 15f).

It is important to clarify that the TDR analyses (Figs. 15a,b,d,e) are constructed over a period of 30–60 min, while the plane traverses the TC vortex, whereas the LFR composites shown in Figs. 15c and 15f use an averaging period of 4 min. Consequently, some small radial and azimuthal displacements in the locations of the banded vorticity and reflectivity structures may exist due to advective processes that occur while the TDR analyses are being constructed. Despite this caveat, the TDR–LFR synthesis exhibits general agreement in the locations of the banded structures and the TC eyewall. The spiral, banded structures of reflectivity and vorticity seen in Fig. 15 are consistent with prior work on VRWs (Montgomery and Kallenbach 1997; Reasor et al. 2000; Corbosiero et al. 2006; Moon and Nolan 2015; Guimond et al. 2019, manuscript submitted to *J. Atmos. Sci.*).

Figure 16 shows the evolution of the banded reflectivity structures immediately outward of the eyewall, as observed by the LFR. The brief time periods shown in Fig. 16 were selected to ensure the plane was near enough to the TC center to avoid appreciable attenuation of the radar beam. Figures 16a and 16b show time–azimuth sections of composite reflectivity taken along the radii encircled by the dashed magenta lines in Figs. 15c and 15f, respectively. If the aforementioned spiral bands of enhanced reflectivity and vorticity are indeed VRWs, they should exhibit characteristics of retrogression relative to the background vortex flow (Montgomery and Kallenbach 1997; Corbosiero et al. 2006).

Near the time of SEF I, a band of enhanced reflectivity at a radius of 25 km, just outside the eyewall, was observed to propagate cyclonically downwind (Fig. 16a). The band was first observed on the southwestern side of the vortex, with peak reflectivities traveling approximately  $65^\circ$  cyclonically downwind over the 18-min observing window. This corresponds to an azimuthal phase speed of approximately  $26 \text{ m s}^{-1}$ . At this time,  $\bar{V}_T$  at a radius of 25 km and a height of 2.5 km, near the flight-level height, was  $49 \text{ m s}^{-1}$  (Fig. 7b), indicating the observed spiral band was retrogressing relative to the mean flow.

Similar azimuthal propagation characteristics were observed near the time of SEF II (Fig. 16b). Here, multiple maxima in composite reflectivity were observed to propagate cyclonically around the southern side of the TC, consistent with the spiral bands extending from the eyewall of the TC as seen in Fig. 15f. Although some small differences in the azimuthal phase speed of these reflectivity maxima exist, even the most rapidly propagating maximum, beginning south-southwest of the TC center, orbits cyclonically nearly  $60^\circ$  in the 18-min interval. This corresponds to an azimuthal phase speed of approximately  $39 \text{ m s}^{-1}$ , which is less than the background  $\bar{V}_T$  value of  $51 \text{ m s}^{-1}$  at a radius of 40 km and a height of 2.5 km (Fig. 9a). Considering the other reflectivity maxima were moving slower than this band, each of these spiral bands were observed to be retrogressing relative to the background vortex flow.

The characteristics of the spiral, inner-core rainbands examined herein are consistent with theoretical work (Montgomery and Kallenbach 1997), numerical modeling

studies (Wang 2002a,b; Qiu et al. 2010; Moon and Nolan 2015), and previous observational studies (Corbosiero et al. 2006) of VRW activity. Thus, we hypothesize the inner-core spiral bands observed near the times of SEF I and SEF II were associated with VRWs. In both SEF events examined here, it appears plausible the eventual stagnation and axisymmetrization of the ongoing VRW activity may have contributed to SEF. Although not shown here, estimates of the theoretical VRW stagnation radius, following methods similar to Reasor et al. (2000), suggest the stagnation radius resided close to the radial locations of both SEF I and SEF II.

## 7. Discussion

### a. Different pathways to SEF

Despite occurring less than 24 h apart, the two SEF events in Hurricane Irma demonstrate that multiple mechanisms can contribute to the formation of a secondary eyewall. The characteristics associated with SEF I displayed many similarities to the SEF event in Hurricane Earl (2010) examined by Didlake et al. (2018), as a local maximum in both ascent and tangential wind developed in a region of enhanced lower-tropospheric convergence near the leading edge of the descending inflow jet, maximized in the downshear-left quadrant of the storm (Fig. 13). During SEF II, however, the same features were not observed in the downshear-left quadrant of Hurricane Irma. This result suggests a mesoscale descending inflow jet is a plausible, but not necessary ingredient for SEF.

In both SEF events, a broadening of the  $\overline{V_T}$  field was observed (Figs. 7 and 9). A radial expansion of the TC vortex, and thus a broadening of the inertial stability field, has been argued to increase the efficiency of the generation of kinetic energy from diabatic heating in a developing outer eyewall (Rozoff et al. 2012; Zhang et al. 2017); however, as suggested by Smith and Montgomery (2016), issues arise when applying efficiency arguments to nonidealized TCs. Namely, efficiency-based hypotheses often assume fixed diabatic heating rates and neglect boundary layer influences. Alternatively, a broadening of the TC vortex has been hypothesized to initiate SEF through supergradient boundary layer flow and agradient forcing (e.g., Huang et al. 2012; Abarca et al. 2016; Huang et al. 2018). The  $\overline{V_R}$  field during SEF II, as measured by the TDR (Fig. 10), was consistent with supergradient flow, with a pronounced corner-flow region located above, and at the leading edge of, robust boundary layer inflow (e.g., Smith and Montgomery 2015).

Unfortunately, the lack of detailed observations of Hurricane Irma's three-dimensional mass field prevents

the direct computation of both the gradient wind as well as a potential agradient force. Furthermore, the vertical resolution of the TDR observations, particularly near the ocean surface, does not allow for a detailed analysis of the inflow structure within the boundary layer. Therefore, some uncertainty exists in regard to the role of unbalanced boundary layer processes—or lack thereof—in the two SEF events examined in this study. Despite these caveats, the TC vortex structure observed during SEF II is consistent with the vortex evolution described by Huang et al. (2012), Abarca et al. (2016), Huang et al. (2018), and others. Considering the observational limitations of this dataset, we cannot discount the potential for unbalanced boundary layer processes to have also contributed to SEF I.

Considering the aforementioned mechanisms and caveats, we hypothesize SEF I was initiated via a mesoscale descending inflow jet associated with a rainband region in the downshear-left quadrant of the storm. Similar to the hypotheses of Didlake and Houze (2013b) and Didlake et al. (2018), it is thought that boundary layer convergence near the leading edge of the descending inflow jet fueled a sustained updraft which generated a local  $V_T$  maximum. The eventual axisymmetrization of this local  $V_T$  maximum is hypothesized to have, at least in part, contributed to SEF I. SEF I may have been aided by the axisymmetrization of outward-propagating VRWs emanating away from the elliptical eyewall. Alternatively, we hypothesize SEF II was initiated through a combination of axisymmetrizing VRWs and enhanced lower-tropospheric convergence related to unbalanced boundary layer processes, both of which were found within a 40–50-km radial band and coincided with a secondary ascent maximum (Figs. 14 and 15d–f).

The hypothesized pathways to SEF likely depend on the convective nature of the TC. Specifically, the mesoscale descending inflow jet observed in SEF I is driven by evaporational cooling from stratiform precipitation (Didlake et al. 2018), while the presumed supergradient flow near the top of the boundary layer, the deeper lower-tropospheric inflow, and the more intense TC vortex observed around the time of SEF II are consistent with more intense convection. The relationship between the convective nature of the TC and SEF was evaluated in the form of contoured frequency by altitude diagrams (CFADs) of vertical velocity ( $V_w$ ), as sampled by the TDR (Fig. 17). Two prominent differences in the distributions of  $V_w$  for SEF I (Fig. 17a) and SEF II (Fig. 17b) exist. The first difference is related to a shift in the mode of  $V_w$ , at all heights, at the time of SEF II to slightly lower values compared to the distribution near the time of SEF I (Fig. 17c). The second difference is

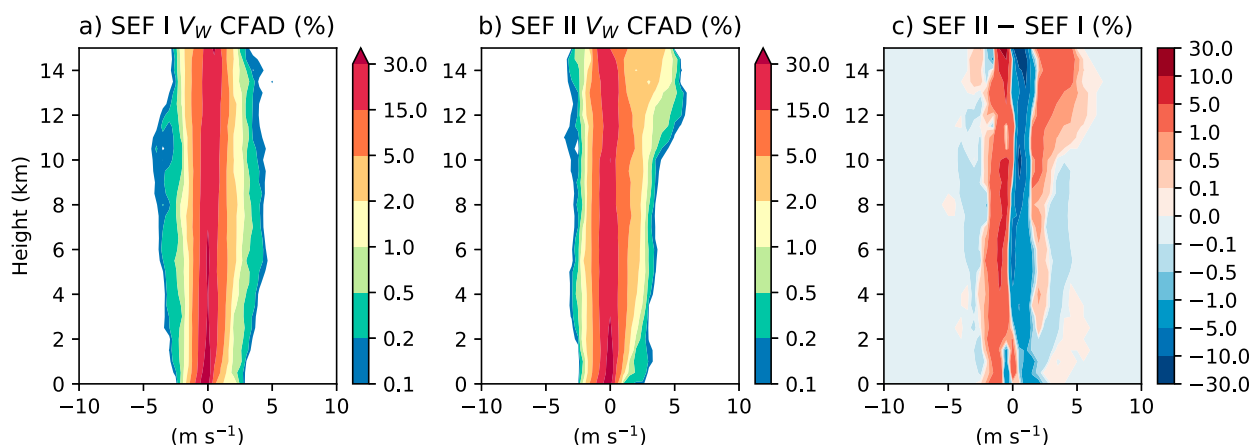


FIG. 17. (a) Contoured frequency by altitude (CFAD) diagram of vertical velocity ( $V_W$ ; %) using values within 150 km of the TC center for the 0904 UTC 4 Sep center pass, near the time of SEF I. Values are binned in increments of  $0.5 \text{ m s}^{-1}$ . (b) As in (a), but using the 0149 UTC 5 Sep center pass, near the time of SEF II. (c) The CFAD difference between (b) and (a). Here, positive values indicate the time near SEF II had a greater frequency of a given  $V_W$  value than the time near SEF I.

found at heights above 8–10 km, as SEF II is associated with a greater frequency of vertical velocities  $>2 \text{ m s}^{-1}$  (Fig. 17c). The more robust updrafts in the upper troposphere observed near the time of SEF II indicate more vigorous, deep convective activity, when compared to SEF I. This result supports the hypothesis that the pathway to SEF displays some dependence to the convective nature of the TC. Although not shown here, similar CFAD analyses were performed using TDR observations from center passes just prior to the times of SEF I and SEF II, and yielded similar results. Nonetheless, some uncertainty remains since these CFADs were constructed using swaths of observations taken at a few different snapshots in time.

#### b. A comparison of the TC vortex evolution during ERC I and ERC II

Following SEF, the two ERC events were also associated with differing vortex evolutions. ERC I displayed a more typical evolution, characterized by the decay of the inner eyewall while the outer eyewall intensified, which induced a temporary decrease in the azimuthally averaged lower-tropospheric winds (Fig. 5); however, the TC intensity continued to increase during this period according to best track estimates (Fig. 1). This discrepancy may be partially attributed to a temporal smoothing of the observations utilized within the best track, although the minimum central pressure measured by aircraft continued to fall between each center pass during this period.

ERC II displayed an atypical vortex evolution. Although the inner eyewall began to decay during ERC II, the two eyewalls appeared to merge together before the inner eyewall could dissipate (Figs. 9 and 11).

The merging of the eyewalls may stem from the smaller displacement between the primary and secondary eyewalls following SEF II, as well as the lack of a well-defined moat between the eyewalls (Zhu and Zhu 2015; Tyner et al. 2018). The continued intensification of the TC vortex during ERC II renders the event as a stark contrast to the ERC paradigm discussed within the literature (Sitkowski et al. 2011).

#### c. Multiscale nature of TC intensification

The RI of Hurricane Irma is a prime example of the complexities associated with the multiscale nature of TC intensification, as evidenced by the interaction of the environmental, vortex, and convective characteristics of the storm. For example, according to SHIPS analyses, Irma was located in an environment of favorable vertical wind shear magnitudes over a period of several days leading up the RI event (Fig. 3a); however, greater intensification rates were not realized until the TC moved over increasing SSTs and ocean heat content. As Irma encountered warmer waters, convective rainband activity also increased (Figs. 6a–c), and ERC I ensued. Contrary to best track estimates, airborne radar observations indicate the  $\bar{V}_T$  field did not begin to rapidly intensify until the completion of ERC I, and instead, the  $\bar{V}_T$  field experienced a temporary weakening during the ERC. Once RI began, the TC secondary circulation also intensified, with the presumably unbalanced boundary layer leading to a second ERC event. In other words, the increasingly favorable environment facilitated the mature-stage RI period, which primed the TC vortex for an additional ERC event, albeit one of an uncommon evolution.

A potential caveat to the aforementioned relationship between RI and the environment is found in the



uncertainty of the estimates. In particular, airborne radar estimates of the local shear were, at times, around  $5 \text{ m s}^{-1}$  larger than operational model analyses (Fig. 12). Although a temporary decrease in the local shear was observed around the time of RI onset, estimates remained in the moderate (e.g.,  $5\text{--}10 \text{ m s}^{-1}$ ) range throughout the remainder of the RI period. Considering previous work has shown TC intensification displays decreased predictability within such a shear regime (e.g., Zhang and Tao 2013), the results shown here emphasize the importance of accurate environmental observations when predicting TC intensity change.

## 8. Conclusions

The initiation of an RI event for a TC at major hurricane intensity is a rare event in the North Atlantic basin. This study examined the environmental and vortex-scale processes related to such an RI event through an observational analysis of Hurricane Irma. The evolution of the TC vortex during RI was examined using both in situ and TDR aircraft reconnaissance observations as well as microwave satellite data. The main findings of this study are highlighted below:

- Two ERC episodes were observed during the RI of Hurricane Irma. The presence of multiple ERCs during a sustained RI event opposes the conceptual model within the literature that links ERCs to a period of weakening or, at the most, steady-state intensity (e.g., Sitkowski et al. 2011; Dougherty et al. 2018).
- The two ERC events were hypothesized to feature different pathways to SEF. The first SEF event was linked to lower-tropospheric convergence along the leading edge of a descending inflow jet in the downshear-left quadrant of the TC. The second SEF event appeared to have originated from lower-tropospheric convergence associated with a presumed supergradient flow. In both events, it is plausible SEF was aided by the axisymmetrization of outward-propagating VRWs near the theoretical stagnation radius.
- ERC I exhibited a relatively common vortex evolution, as the inner eyewall decayed at the expense of an intensifying outer eyewall. Although not reflected in the best track analysis, aircraft reconnaissance observations indicated a brief weakening of the maximum tangential wind throughout the lower troposphere. Alternatively, during ERC II, the two eyewalls appeared to merge together prior to the collapse of the inner eyewall, with no signs of the vortex weakening.
- In each ERC, the time elapsed between the formation of a secondary wind maximum to the completion of the ERC was  $<12 \text{ h}$ . This time period is significantly

less than the mean ERC duration of 36 h (Sitkowski et al. 2011). Additionally, both ERCs featured a relatively small initial displacement between the primary and secondary eyewall (20–40 km), which is substantially less than the climatological mean of 71 km.

The possibility of an ERC to not induce a period of weakening in the TC has important implications for human impacts. In both ERCs analyzed here, a temporary expansion of the RMW was observed following the completion of the ERC event. A larger RMW would not only bring the most damaging winds over a larger area, but has also been shown to cause greater storm surge inundation (Irish et al. 2008; Lin et al. 2014). The TC intensity evolution observed during ERC II—and to some extent, ERC I—demonstrates a forecaster should not necessarily assume a period of steady-state intensity or weakening will commence following the appearance of a secondary eyewall.

A naturally arising question can be posed: How did Irma continue to experience RI during ERC II? We hypothesize the persistent ascent radially inward of the primary eyewall was associated with the inward advection of relatively large angular momentum surfaces, along the lines of Montgomery and Smith (2014), Smith and Montgomery (2015), Smith and Montgomery (2016), and others. The persistence of this ascent was maintained by both a region of weak inflow seen above the corner-flow region near the top of the boundary layer, as well as the rapid pace of the ERC, which did not allow a significant amount of time for the inner eyewall to weaken prior to the eventual eyewall merger. Although a more quantitative analysis is ideal, the present study was limited by the intermittent sampling and the spatial resolution of the observational datasets. Future work will utilize representative high-resolution modeling simulations to gain a better understanding of the relationship between TC intensity change and the rapidly evolving vortex structure during the ERCs analyzed here.

The results of this study also raise other questions. For example, if ERC II was initiated by the convergence between the TC inflow layer and a corner-flow region, why do not all TCs that exhibit such supergradient flow experience SEF? Numerical simulations of Typhoon Sinlaku (2008) analyzed by Huang et al. (2012) suggest SEF occurs once boundary layer convergence associated with supergradient flow becomes increasingly persistent and exceeds a threshold value; however, it is challenging to test such a hypothesis using observations. In the case of Irma, ERC II was only detected due to the relatively high frequency of aircraft reconnaissance missions flown into the TC, as microwave satellite observations failed to

detect the ERC. The results provided here not only underscore the utility of aircraft reconnaissance observations in studying TC intensity and structural changes, but also demonstrate the need for a more detailed observational network in the TC boundary layer. It is possible other TCs have exhibited vortex evolutions similar to ERC II, but were missed by satellite-based observing systems. The environmental conditions and predecessor vortex structures favoring a vortex evolution similar to ERC II need to be explored in more detail considering the TC intensity and inner-core size changes associated with such ERCs, which can compound societal impacts if the ERC precedes landfall.

**Acknowledgments.** The constructive and enlightening comments of Drs. Michael Montgomery, Frank Marks, Jun Zhang, and two anonymous reviewers improved the quality and clarity of this analysis. The authors thank John Kaplan for helpful discussions about environmental influences on Irma's intensity evolution and Dr. Christopher Rozoff for providing the microwave brightness temperatures. Conversations with Drs. Anthony Didlake and Xiaomin Chen also provided valuable insight into this analysis. The first author was supported by the National Research Council Research Associateship Programs.

#### REFERENCES

- Abarca, S. F., and K. L. Corbosiero, 2011: Secondary eyewall formation in WRF simulations of Hurricanes Rita and Katrina (2005). *Geophys. Res. Lett.*, **38**, L07802, <https://doi.org/10.1029/2011GL047015>.
- , and M. T. Montgomery, 2013: Essential dynamics of secondary eyewall formation. *J. Atmos. Sci.*, **70**, 3216–3230, <https://doi.org/10.1175/JAS-D-12-0318.1>.
- , —, S. A. Braun, and J. Dunion, 2016: On the secondary eyewall formation of Hurricane Edouard (2014). *Mon. Wea. Rev.*, **144**, 3321–3331, <https://doi.org/10.1175/MWR-D-15-0421.1>.
- Bell, M. M., and M. T. Montgomery, 2008: Observed structure, evolution, and potential intensity of category 5 Hurricane Isabel (2003) from 12 to 14 September. *Mon. Wea. Rev.*, **136**, 2023–2046, <https://doi.org/10.1175/2007MWR1858.1>.
- , —, and W.-C. Lee, 2012: An axisymmetric view of concentric eyewall evolution in Hurricane Rita (2005). *J. Atmos. Sci.*, **69**, 2414–2432, <https://doi.org/10.1175/JAS-D-11-0167.1>.
- Black, M. L., and H. E. Willoughby, 1992: The concentric eyewall cycle of Hurricane Gilbert. *Mon. Wea. Rev.*, **120**, 947–957, [https://doi.org/10.1175/1520-0493\(1992\)120<0947:TCECOH>2.0.CO;2](https://doi.org/10.1175/1520-0493(1992)120<0947:TCECOH>2.0.CO;2).
- Bosart, L. F., W. E. Bracken, J. Molinari, C. S. Velden, and P. G. Black, 2000: Environmental influences on the rapid intensification of Hurricane Opal (1995) over the Gulf of Mexico. *Mon. Wea. Rev.*, **128**, 322–352, [https://doi.org/10.1175/1520-0493\(2000\)128<0322:EIOTRI>2.0.CO;2](https://doi.org/10.1175/1520-0493(2000)128<0322:EIOTRI>2.0.CO;2).
- Cangialosi, J. P., A. S. Lotto, and R. Berg, 2018: National Hurricane Center tropical cyclone report: Hurricane Irma (30 August–12 September 2017). NHC Rep. AL112017, 111 pp, [https://www.nhc.noaa.gov/data/tcr/AL112017\\_Irma.pdf](https://www.nhc.noaa.gov/data/tcr/AL112017_Irma.pdf).
- Cecil, D. J., and E. J. Zipser, 1999: Relationships between tropical cyclone intensity and satellite-based indicators of inner core convection: 85-GHz ice-scattering signature and lightning. *Mon. Wea. Rev.*, **127**, 103–123, [https://doi.org/10.1175/1520-0493\(1999\)127<0103:RBTCIA>2.0.CO;2](https://doi.org/10.1175/1520-0493(1999)127<0103:RBTCIA>2.0.CO;2).
- Chen, S. S., J. A. Knaff, and F. D. Marks, 2006: Effects of vertical wind shear and storm motion on tropical cyclone rainfall asymmetries deduced from TRMM. *Mon. Wea. Rev.*, **134**, 3190–3208, <https://doi.org/10.1175/MWR3245.1>.
- Corbosiero, K. L., and J. Molinari, 2002: The effects of vertical wind shear on the distribution of convection in tropical cyclones. *Mon. Wea. Rev.*, **130**, 2110–2123, [https://doi.org/10.1175/1520-0493\(2002\)130<2110:TEOVWS>2.0.CO;2](https://doi.org/10.1175/1520-0493(2002)130<2110:TEOVWS>2.0.CO;2).
- , —, A. R. Aiyyer, and M. L. Black, 2006: The structure and evolution of Hurricane Elena (1985). Part II: Convective asymmetries and evidence for vortex Rossby waves. *Mon. Wea. Rev.*, **134**, 3073–3091, <https://doi.org/10.1175/MWR3250.1>.
- Dai, Y., S. J. Majumdar, and D. S. Nolan, 2017: Secondary eyewall formation in tropical cyclones by outflow-jet interaction. *J. Atmos. Sci.*, **74**, 1941–1958, <https://doi.org/10.1175/JAS-D-16-0322.1>.
- DeHart, J. C., R. A. Houze, and R. F. Rogers, 2014: Quadrant distribution of tropical cyclone inner-core kinematics in relation to environmental shear. *J. Atmos. Sci.*, **71**, 2713–2732, <https://doi.org/10.1175/JAS-D-13-0298.1>.
- DeMaria, M., and J. Kaplan, 1994: A Statistical Hurricane Intensity Prediction Scheme (SHIPS) for the Atlantic basin. *Wea. Forecasting*, **9**, 209–220, [https://doi.org/10.1175/1520-0434\(1994\)009<0209:ASHIPS>2.0.CO;2](https://doi.org/10.1175/1520-0434(1994)009<0209:ASHIPS>2.0.CO;2).
- , C. R. Sampson, J. A. Knaff, and K. D. Musgrave, 2014: Is tropical cyclone intensity guidance improving? *Bull. Amer. Meteor. Soc.*, **95**, 387–398, <https://doi.org/10.1175/BAMS-D-12-00240.1>.
- Didlake, A. C., and R. A. Houze, 2013a: Convective-scale variations in the inner-core rainbands of a tropical cyclone. *J. Atmos. Sci.*, **70**, 504–523, <https://doi.org/10.1175/JAS-D-12-0134.1>.
- , and —, 2013b: Dynamics of the stratiform sector of a tropical cyclone rainband. *J. Atmos. Sci.*, **70**, 1891–1911, <https://doi.org/10.1175/JAS-D-12-0245.1>.
- , P. D. Reasor, R. F. Rogers, and W.-C. Lee, 2018: Dynamics of the transition from spiral rainbands to a secondary eyewall in Hurricane Earl (2010). *J. Atmos. Sci.*, **75**, 2909–2929, <https://doi.org/10.1175/JAS-D-17-0348.1>.
- Dougherty, E. M., J. Molinari, R. F. Rogers, J. A. Zhang, and J. P. Kossin, 2018: Hurricane Bonnie (1998): Maintaining intensity during high vertical wind shear and an eyewall replacement cycle. *Mon. Wea. Rev.*, **146**, 3383–3399, <https://doi.org/10.1175/MWR-D-18-0030.1>.
- Fang, J., and F. Zhang, 2012: Effect of beta shear on simulated tropical cyclones. *Mon. Wea. Rev.*, **140**, 3327–3346, <https://doi.org/10.1175/MWR-D-10-05021.1>.
- Fischer, M. S., B. H. Tang, and K. L. Corbosiero, 2017: Assessing the influence of upper-tropospheric troughs on tropical cyclone intensification rates after genesis. *Mon. Wea. Rev.*, **145**, 1295–1313, <https://doi.org/10.1175/MWR-D-16-0275.1>.
- Gall, R., J. Franklin, F. Marks, E. N. Rappaport, and F. Toepfer, 2013: The Hurricane Forecast Improvement Project. *Bull. Amer. Meteor. Soc.*, **94**, 329–343, <https://doi.org/10.1175/BAMS-D-12-00071.1>.
- Gao, J., M. Xue, A. Shapiro, and K. K. Droegemeier, 1999: A variational method for the analysis of three-dimensional

- wind fields from two Doppler radars. *Mon. Wea. Rev.*, **127**, 2128–2142, [https://doi.org/10.1175/1520-0493\(1999\)127<2128:AVMFTA>2.0.CO;2](https://doi.org/10.1175/1520-0493(1999)127<2128:AVMFTA>2.0.CO;2).
- Hence, D. A., and R. A. Houze, 2012: Vertical structure of tropical cyclone rainbands as seen by the TRMM precipitation radar. *J. Atmos. Sci.*, **69**, 2644–2661, <https://doi.org/10.1175/JAS-D-11-0323.1>.
- Hendricks, E. A., M. S. Peng, B. Fu, and T. Li, 2010: Quantifying environmental control on tropical cyclone intensity change. *Mon. Wea. Rev.*, **138**, 3243–3271, <https://doi.org/10.1175/2010MWR3185.1>.
- Houze, R. A., 2010: Clouds in tropical cyclones. *Mon. Wea. Rev.*, **138**, 293–344, <https://doi.org/10.1175/2009MWR2989.1>.
- , S. S. Chen, B. F. Smull, W.-C. Lee, and M. M. Bell, 2007: Hurricane intensity and eyewall replacement. *Science*, **315**, 1235–1239, <https://doi.org/10.1126/science.1135650>.
- Huang, Y.-H., M. T. Montgomery, and C.-C. Wu, 2012: Concentric eyewall formation in Typhoon Sinlaku (2008). Part II: Axisymmetric dynamical processes. *J. Atmos. Sci.*, **69**, 662–674, <https://doi.org/10.1175/JAS-D-11-0114.1>.
- , C.-C. Wu, and M. T. Montgomery, 2018: Concentric eyewall formation in Typhoon Sinlaku (2008). Part III: Horizontal momentum budget analyses. *J. Atmos. Sci.*, **75**, 3541–3563, <https://doi.org/10.1175/JAS-D-18-0037.1>.
- Irish, J. L., D. T. Resio, and J. J. Ratcliff, 2008: The influence of storm size on hurricane surge. *J. Phys. Oceanogr.*, **38**, 2003–2013, <https://doi.org/10.1175/2008JPO3727.1>.
- Judt, F., and S. S. Chen, 2010: Convectively generated potential vorticity in rainbands and formation of the secondary eyewall in Hurricane Rita of 2005. *J. Atmos. Sci.*, **67**, 3581–3599, <https://doi.org/10.1175/2010JAS3471.1>.
- , and —, 2016: Predictability and dynamics of tropical cyclone rapid intensification deduced from high-resolution stochastic ensembles. *Mon. Wea. Rev.*, **144**, 4395–4420, <https://doi.org/10.1175/MWR-D-15-0413.1>.
- Kaplan, J., and M. DeMaria, 2003: Large-scale characteristics of rapidly intensifying tropical cyclones in the North Atlantic basin. *Wea. Forecasting*, **18**, 1093–1108, [https://doi.org/10.1175/1520-0434\(2003\)018<1093:LCORIT>2.0.CO;2](https://doi.org/10.1175/1520-0434(2003)018<1093:LCORIT>2.0.CO;2).
- , and Coauthors, 2015: Evaluating environmental impacts on tropical cyclone rapid intensification predictability utilizing statistical models. *Wea. Forecasting*, **30**, 1374–1396, <https://doi.org/10.1175/WAF-D-15-0032.1>.
- Kepernt, J. D., 2013: How does the boundary layer contribute to eyewall replacement cycles in axisymmetric tropical cyclones? *J. Atmos. Sci.*, **70**, 2808–2830, <https://doi.org/10.1175/JAS-D-13-046.1>.
- , and D. S. Nolan, 2014: Reply to “Comments on ‘How does the boundary layer contribute to eyewall replacement cycles in axisymmetric tropical cyclones?’” *J. Atmos. Sci.*, **71**, 4692–4704, <https://doi.org/10.1175/JAS-D-14-0014.1>.
- Kossin, J. P., and M. Sitkowski, 2009: An objective model for identifying secondary eyewall formation in hurricanes. *Mon. Wea. Rev.*, **137**, 876–892, <https://doi.org/10.1175/2008MWR2701.1>.
- , and —, 2012: Predicting hurricane intensity and structure changes associated with eyewall replacement cycles. *Wea. Forecasting*, **27**, 484–488, <https://doi.org/10.1175/WAF-D-11-00106.1>.
- , and M. DeMaria, 2016: Reducing operational hurricane intensity forecast errors during eyewall replacement cycles. *Wea. Forecasting*, **31**, 601–608, <https://doi.org/10.1175/WAF-D-15-0123.1>.
- Leroux, M.-D., M. Plu, D. Barbary, F. Roux, and P. Arbogast, 2013: Dynamical and physical processes leading to tropical cyclone intensification under upper-level trough forcing. *J. Atmos. Sci.*, **70**, 2547–2565, <https://doi.org/10.1175/JAS-D-12-0293.1>.
- Lin, N., P. Lane, K. A. Emanuel, R. M. Sullivan, and J. P. Donnelly, 2014: Heightened hurricane surge risk in northwest Florida revealed from climatological-hydrodynamic modeling and paleorecord reconstruction. *J. Geophys. Res. Atmos.*, **119**, 8606–8623, <https://doi.org/10.1002/2014JD021584>.
- Mohr, K. I., and E. J. Zipser, 1996a: Defining mesoscale convective systems by their 85-GHz ice-scattering signatures. *Bull. Amer. Meteor. Soc.*, **77**, 1179–1189, [https://doi.org/10.1175/1520-0477\(1996\)077<1179:DMCSBT>2.0.CO;2](https://doi.org/10.1175/1520-0477(1996)077<1179:DMCSBT>2.0.CO;2).
- , and —, 1996b: Mesoscale convective systems defined by their 85-GHz ice scattering signature: Size and intensity comparison over tropical oceans and continents. *Mon. Wea. Rev.*, **124**, 2417–2437, [https://doi.org/10.1175/1520-0493\(1996\)124<2417:MCSDBT>2.0.CO;2](https://doi.org/10.1175/1520-0493(1996)124<2417:MCSDBT>2.0.CO;2).
- , R. Toracinta, E. J. Zipser, and R. E. Orville, 1996: A comparison of WSR-88D reflectivities, SSM/I brightness temperatures, and lightning for mesoscale convective systems in Texas. Part II: SSM/I brightness temperatures and lightning. *J. Appl. Meteor.*, **35**, 919–931, [https://doi.org/10.1175/1520-0450\(1996\)035<0919:ACOWRS>2.0.CO;2](https://doi.org/10.1175/1520-0450(1996)035<0919:ACOWRS>2.0.CO;2).
- Molinari, J., and D. Vollaro, 1989: External influences on hurricane intensity. Part I: Outflow layer eddy angular momentum fluxes. *J. Atmos. Sci.*, **46**, 1093–1105, [https://doi.org/10.1175/1520-0469\(1989\)046<1093:EIOHIP>2.0.CO;2](https://doi.org/10.1175/1520-0469(1989)046<1093:EIOHIP>2.0.CO;2).
- , and —, 1990: External influences on hurricane intensity. Part II: Vertical structure and response of the hurricane vortex. *J. Atmos. Sci.*, **47**, 1902–1918, [https://doi.org/10.1175/1520-0469\(1990\)047<1902:EIOHIP>2.0.CO;2](https://doi.org/10.1175/1520-0469(1990)047<1902:EIOHIP>2.0.CO;2).
- Montgomery, M. T., and R. J. Kallenbach, 1997: A theory for vortex Rossby-waves and its application to spiral bands and intensity changes in hurricanes. *Quart. J. Roy. Meteor. Soc.*, **123**, 435–465, <https://doi.org/10.1002/qj.49712353810>.
- , and R. K. Smith, 2014: Paradigms for tropical cyclone intensification. *Aust. Meteor. Oceanogr. J.*, **64**, 37–66, <https://doi.org/10.22499/2.6401.005>.
- Montgomery, M. T., S. Abarca, R. Smith, C. Wu, and Y. Huang, 2014a: Comments on “How does the boundary layer contribute to eyewall replacement cycles in axisymmetric tropical cyclones?” *J. Atmos. Sci.*, **71**, 4682–4691, <https://doi.org/10.1175/JAS-D-13-0286.1>.
- Montgomery, M. T., J. A. Zhang, and R. K. Smith, 2014b: An analysis of the observed low-level structure of rapidly intensifying and mature Hurricane Earl. *Quart. J. Roy. Meteor. Soc.*, **140**, 2132–2146, <https://doi.org/10.1002/qj.2283>.
- Moon, Y., and D. S. Nolan, 2015: Spiral rainbands in a numerical simulation of Hurricane Bill (2009). Part II: Propagation of inner rainbands. *J. Atmos. Sci.*, **72**, 191–215, <https://doi.org/10.1175/JAS-D-14-0056.1>.
- Nong, S., and K. Emanuel, 2003: A numerical study of the genesis of concentric eyewalls in hurricanes. *Quart. J. Roy. Meteor. Soc.*, **129**, 3323–3338, <https://doi.org/10.1256/qj.01.132>.
- Qiu, X., Z.-M. Tan, and Q. Xiao, 2010: The roles of vortex Rossby waves in hurricane secondary eyewall formation. *Mon. Wea. Rev.*, **138**, 2092–2109, <https://doi.org/10.1175/2010MWR3161.1>.
- Reasor, P. D., and M. D. Eastin, 2012: Rapidly intensifying Hurricane Guillermo (1997). Part II: Resilience in shear. *Mon. Wea. Rev.*, **140**, 425–444, <https://doi.org/10.1175/MWR-D-11-00080.1>.

- , M. T. Montgomery, F. D. Marks, and J. F. Gamache, 2000: Low-wavenumber structure and evolution of the hurricane inner core observed by airborne dual-Doppler radar. *Mon. Wea. Rev.*, **128**, 1653–1680, [https://doi.org/10.1175/1520-0493\(2000\)128<1653:LWSAEO>2.0.CO;2](https://doi.org/10.1175/1520-0493(2000)128<1653:LWSAEO>2.0.CO;2).
- , M. D. Eastin, and J. F. Gamache, 2009: Rapidly intensifying Hurricane Guillermo (1997). Part I: Low-wavenumber structure and evolution. *Mon. Wea. Rev.*, **137**, 603–631, <https://doi.org/10.1175/2008MWR2487.1>.
- , R. Rogers, and S. Lorsolo, 2013: Environmental flow impacts on tropical cyclone structure diagnosed from airborne Doppler radar composites. *Mon. Wea. Rev.*, **141**, 2949–2969, <https://doi.org/10.1175/MWR-D-12-00334.1>.
- Riemer, M., M. T. Montgomery, and M. E. Nicholls, 2010: A new paradigm for intensity modification of tropical cyclones: Thermodynamic impact of vertical wind shear on the inflow layer. *Atmos. Chem. Phys.*, **10**, 3163–3188, <https://doi.org/10.5194/acp-10-3163-2010>.
- Rogers, R., S. Lorsolo, P. Reasor, J. Gamache, and F. Marks, 2012: Multiscale analysis of tropical cyclone kinematic structure from airborne Doppler radar composites. *Mon. Wea. Rev.*, **140**, 77–99, <https://doi.org/10.1175/MWR-D-10-05075.1>.
- , P. Reasor, and S. Lorsolo, 2013: Airborne Doppler observations of the inner-core structural differences between intensifying and steady-state tropical cyclones. *Mon. Wea. Rev.*, **141**, 2970–2991, <https://doi.org/10.1175/MWR-D-12-00357.1>.
- , —, and J. A. Zhang, 2015: Multiscale structure and evolution of Hurricane Earl (2010) during rapid intensification. *Mon. Wea. Rev.*, **143**, 536–562, <https://doi.org/10.1175/MWR-D-14-00175.1>.
- Rozoff, C. M., W. H. Schubert, and J. P. Kossin, 2008: Some dynamical aspects of tropical cyclone concentric eyewalls. *Quart. J. Roy. Meteor. Soc.*, **134**, 583–593, <https://doi.org/10.1002/qj.237>.
- , D. S. Nolan, J. P. Kossin, F. Zhang, and J. Fang, 2012: The roles of an expanding wind field and inertial stability in tropical cyclone secondary eyewall formation. *J. Atmos. Sci.*, **69**, 2621–2643, <https://doi.org/10.1175/JAS-D-11-0326.1>.
- , C. S. Velden, J. Kaplan, J. P. Kossin, and A. J. Wimmers, 2015: Improvements in the probabilistic prediction of tropical cyclone rapid intensification with passive microwave observations. *Wea. Forecasting*, **30**, 1016–1038, <https://doi.org/10.1175/WAF-D-14-00109.1>.
- Shapiro, L. J., and H. E. Willoughby, 1982: The response of balanced hurricanes to local sources of heat and momentum. *J. Atmos. Sci.*, **39**, 378–394, [https://doi.org/10.1175/1520-0469\(1982\)039<0378:TROBHT>2.0.CO;2](https://doi.org/10.1175/1520-0469(1982)039<0378:TROBHT>2.0.CO;2).
- Sitkowski, M., J. P. Kossin, and C. M. Rozoff, 2011: Intensity and structure changes during hurricane eyewall replacement cycles. *Mon. Wea. Rev.*, **139**, 3829–3847, <https://doi.org/10.1175/MWR-D-11-00034.1>.
- Smith, R. K., and M. T. Montgomery, 2015: Toward clarity on understanding tropical cyclone intensification. *J. Atmos. Sci.*, **72**, 3020–3031, <https://doi.org/10.1175/JAS-D-15-0017.1>.
- , and —, 2016: The efficiency of diabatic heating and tropical cyclone intensification. *Quart. J. Roy. Meteor. Soc.*, **142**, 2081–2086, <https://doi.org/10.1002/qj.2804>.
- , —, and N. V. Sang, 2009: Tropical cyclone spin-up revisited. *Quart. J. Roy. Meteor. Soc.*, **135**, 1321–1335, <https://doi.org/10.1002/qj.428>.
- Stern, D. P., and G. H. Bryan, 2018: Using simulated dropsondes to understand extreme updrafts and wind speeds in tropical cyclones. *Mon. Wea. Rev.*, **146**, 3901–3925, <https://doi.org/10.1175/MWR-D-18-0041.1>.
- Terwey, W. D., and M. T. Montgomery, 2008: Secondary eyewall formation in two idealized, full-physics modeled hurricanes. *J. Geophys. Res.*, **113**, D12112, <https://doi.org/10.1029/2007JD008897>.
- Tyner, B., P. Zhu, J. Zhang, S. Gopalakrishnan, F. Marks, and V. Tallapragada, 2018: A top-down pathway to secondary eyewall formation in simulated tropical cyclones. *J. Geophys. Res. Atmos.*, **123**, 174–197, <https://doi.org/10.1002/2017JD027410>.
- Wang, Y., 2002a: Vortex Rossby waves in a numerically simulated tropical cyclone. Part I: Overall structure, potential vorticity, and kinetic energy budgets. *J. Atmos. Sci.*, **59**, 1213–1238, [https://doi.org/10.1175/1520-0469\(2002\)059%3C1213:VRWIAN%3E2.0.co;2](https://doi.org/10.1175/1520-0469(2002)059%3C1213:VRWIAN%3E2.0.co;2).
- , 2002b: Vortex Rossby waves in a numerically simulated tropical cyclone. Part II: The role in tropical cyclone structure and intensity changes. *J. Atmos. Sci.*, **59**, 1239–1262, [https://doi.org/10.1175/1520-0469\(2002\)059<1239:VRWIAN>2.0.CO;2](https://doi.org/10.1175/1520-0469(2002)059<1239:VRWIAN>2.0.CO;2).
- Willoughby, H. E., J. A. Clos, and M. G. Shoreibah, 1982: Concentric eye walls, secondary wind maxima, and the evolution of the hurricane vortex. *J. Atmos. Sci.*, **39**, 395–411, [https://doi.org/10.1175/1520-0469\(1982\)039<0395:CEWSWM>2.0.CO;2](https://doi.org/10.1175/1520-0469(1982)039<0395:CEWSWM>2.0.CO;2).
- , F. D. Marks, and R. J. Feinberg, 1984: Stationary and moving convective bands in hurricanes. *J. Atmos. Sci.*, **41**, 3189–3211, [https://doi.org/10.1175/1520-0469\(1984\)041<3189:SAMCBI>2.0.CO;2](https://doi.org/10.1175/1520-0469(1984)041<3189:SAMCBI>2.0.CO;2).
- Zhang, F., and D. Tao, 2013: Effects of vertical wind shear on the predictability of tropical cyclones. *J. Atmos. Sci.*, **70**, 975–983, <https://doi.org/10.1175/JAS-D-12-0133.1>.
- , —, Y. Q. Sun, and J. D. Kepert, 2017: Dynamics and predictability of secondary eyewall formation in sheared tropical cyclones. *J. Adv. Model. Earth Syst.*, **9**, 89–112, <https://doi.org/10.1002/2016MS000729>.
- Zhu, P., and Coauthors, 2015: Impact of subgrid-scale processes on eyewall replacement cycle of tropical cyclones in HWRF system. *Geophys. Res. Lett.*, **42**, 10 027–10 036, <https://doi.org/10.1002/2015GL066436>.
- Zhu, Z., and P. Zhu, 2015: Sensitivities of eyewall replacement cycle to model physics, vortex structure, and background winds in numerical simulations of tropical cyclones. *J. Geophys. Res. Atmos.*, **120**, 599–622, <https://doi.org/10.1002/2014JD022056>.